International Journal of Fatigue 214 (2027) 109905

Contents lists available at ScienceDirect

International Journal of Fatigue

journal homepage: www.elsevier.com/locate/ijfatigue

Effect of tempering temperatures on the fatigue behavior of 0.6% C martensitic steel

Jiaqiang Dang [a,*], Sien Liu [a], Eisuke Kazama [a], Ryuji Yabutani [a], Karel Blanken [a], Fabien Briffod [b], Shoichi Nambu [a,*]

[a] *Department of Materials Engineering, Graduate School of Engineering, The University of Tokyo, 7-3-1 Hongo, Bunkyo-ku 113-8656, Japan*
[b] *Research Center for Structural Materials, National Institute for Materials Science, 1-2-1 Sengen, Tsukuba, Ibaraki 305-0047, Japan*

A R T I C L E I N F O

Keywords:
0.6% C martensitic steel
Warm tempering
Microstructure
Fracture toughness
Bending fatigue

A B S T R A C T

The martensitic steels have attracted significant attention in various industries due to their superior mechanical properties and fatigue resistance. However, the fatigue behavior of high-carbon martensitic steels remains insufficiently understood. In this study, the effect of tempering process on the fatigue behavior of a 0.6% C martensitic steel was systematically investigated. Three tempering conditions, namely T180, T500 and T650, were applied, resulting in distinct microstructures and mechanical responses. The fatigue performance was elucidated through a combination of crystal plasticity finite element method (CPFEM) and experimental characterization. The results indicate that tempering has a limited effect on grain size while enhanced carbon segregation promotes the formation of dense carbides along boundaries. Carbides and inclusions serve as the primary crack initiation sites regardless of tempering condition, whereas intergranular crack propagation is more pronounced in the low-tempered state. Combined CPFEM and experimental analyses reveal that fracture toughness, governing the main crack formation, plays a critical role in controlling fatigue resistance. Increased fracture toughness at higher tempering temperatures significantly delays the cycles to the main crack formation. However, excessive tempering leads to substantial strength degradation, which increased the potential number of main crack formation sites and deteriorates fatigue resistance.

1. Introduction

The continuous demand for enhanced fatigue resistance in structural components applied in automotive, aerospace, and energy industries has driven the development of advanced high strength steels [1–3]. Among various candidates, martensitic steels have gained appealing attention due to their superior mechanical properties and fatigue resistance [4,5]. Traditionally, quenching and tempering (Q&T) heat treatment is extensively employed by the steel communities during the production of martensitic steels [6]. It has been reported that adjusting desirable quenching method is one of the effective ways to enhance the strength and fatigue behavior of martensitic steels [7]. In addition, the quenching medium which controls the cooling rates during the martensite transformation offered a high possibility to gain better fatigue property [8–10]. However, after quenching, tempering at appropriate temperature also plays an essential role in securing a balance between strength and ductility for martensitic steels, especially for the brittle steel grade with high carbon content [11–13]. To be specific, tempering can reduce the intrinsic residual stress, redistribute dislocations and yield higher plastic deformation with a relatively tolerable loss of strength [14–17]. To sum up, the mechanical properties and fatigue resistance of martensitic steels are greatly dependent on the heat treatment processes [17]. The efforts into understanding the influences of quenching and tempering conditions on microstructures and fatigue behaviors of martensitic steels is of great importance to improve their engineering design technologies for desirable service [18].

In recent years, extensive studies have been performed to improve the mechanical properties and/or fatigue strength of steel grades via effective quenching and tempering processes [19–24]. Dhua et al. [19] investigated the effects of cooling rate on the microstructure and mechanical properties. It was noted that oil or water quenching was recommended in lower thickness plates to enhance the material strength and toughness owing to the closer lath spacing induced by higher cooling rate. Rani et al. [20] concluded that the higher hardness with

* Corresponding authors.
E-mail addresses: jq_dang@metall.t.u-tokyo.ac.jp (J. Dang), nambu@metall.t.u-tokyo.ac.jp (S. Nambu).

https://doi.org/10.1016/j.ijfatigue.2026.109905
Received 28 May 2026; Received in revised form 30 July 2026; Accepted 3 August 2026
Available online 4 August 2026

lower tempering temperature contributed to an enhanced tensile strength as well as fatigue property for martensitic steel with 0.267% C and the effect of tempering temperature is more obvious than that of tempering time. Zhao et al. [21] analyzed the dependence of mechanical properties of martensitic steel with 0.19% C on the tempering temperature and found that an increase in tempering temperature leaded to high fracture toughness with deteriorated tensile strength due to strong recovery and partial recrystallization. Yang et al. [22] investigated the relationship between tempering temperature and low cycle fatigue of a new martensitic steel with 0.21% C. The results indicated that the monotone mechanical properties and fatigue behavior decreased with the increase of tempering temperature and the elevation of lath width, decomposition of residual austenite and decreased dislocations were the primary reasons. Qu et al. [25] studied the tensile properties and rotary bending fatigue of a martensitic steel with 0.188% C and stated that the dislocation density reduced as a result of increased tempering temperature, leading to a lower tensile strength and fatigue limit. As well, it was indicated that the fatigue behavior of a 55NiCrMoV7 steel was reduced with elevated tempering temperature over 500 °C due to the decrease in hardness and the cyclic softening effect [26]. Moreover, Wei et al. [27] concluded that a better combination of strength, fracture toughness and fatigue properties was obtained after tempering at 370 °C compared to that at 280 °C in a steel with 0.22% C.

To date, the relationship between mechanical properties and microstructures subjected to different heat treatments for martensitic steels have been shown in previous studies [26,28–31]. However, most of the attention was paid to the study of martensitic steels with a low carbon from the literature survey. The comprehensive analysis of microstructures and fatigue behavior of martensitic steels with a high carbon in different heat treatment conditions was still rarely explored. It was worth noting that the carbon content showed an appealing influence on the microstructure evolution during the heat treatment, which affected the deformation mechanisms of martensitic steels [32,33]. Therefore, it is necessary to put efforts to studying the microstructures and its relation with the mechanical responses of high carbon martensitic steels under varying heat treatments. In this work, we evaluated the bending fatigue behavior of a martensitic steel with 0.6% C, with special attention paid on the effect of tempering temperatures on the microstructure evolution and mechanical properties. The purpose of this work is to explore how the thermal history during tempering affects the microstructure, mechanical property and fatigue behavior of martensitic steels with high carbon content and further open pathways to achieve exceptional fatigue resistance in such materials. To be specific, the subdomain microstructures and mechanical properties as a function of tempering process were analyzed and emphasis was also made on the mechanisms responsible for the difference in bending fatigue behavior.

2. Materials and experimental procedures

2.1. Materials

The material studied in this work was produced by a hot-rolled sheet with 0.6% carbon referred as 6C provided by Nippon Steel Technology Co. Ltd. and the chemical compositions detected by the company were given in Table 1. The raw steel sheet was cut by wire-electrode into different types of samples for further heat treatment and mechanical tests. The shape and dimensions of the samples studied for various purposes are indicated in Fig. 1. It was worth noting that the length direction of the samples was perpendicular to the rolling direction of the sheet during their preparation. Subsequently, the samples were subjected to different heat treatment processes, with details plotted in Fig. 2. The samples were heated in the furnace at 900 °C for 10 min into austenite, then quenched in oil to induce the martensite subdomain microstructures. After quenching, three types of tempering temperatures including 180 °C, 500 °C, and 650 °C referred as T180, T500 and T650 respectively were utilized to treat the samples for 60 min. In this regard, the intrinsic residual stress produced during quenching process was relieved and the ductility of the martensitic steels was further enhanced. Finally, three groups set as 6C-T180, 6C-T500 and 6C-T650 were involved in this work with aim to address the bending fatigue behavior evolution as a function of tempering process in high carbon martensitic steels.

The samples subjected to the arranged heat treatment conditions were mechanically ground by SiC sandpapers (No. $80^{\#}$, $320^{\#}$, $500^{\#}$, $1000^{\#}$). Each sandpaper was used with a revolution speed of 300 rpm, applied force of 2.5 DaN, and duration time of 180 s. Then, the samples were polished with Al_2O_3 (1 μm) and SiO_2 (0.04 μm) suspensions. Each polishing process was performed with a revolution of 150 rpm, applied force of 2.0 DaN and duration time of 600 s. Starting with the etching by 2% Nital solution, the metallographic microstructure was revealed by a scanning electron microscopy (SEM, JEOL, JSM-7001F), where clear signs of carbide precipitation could be captured. Again, microstructure differences were characterized by electron backscattered diffraction (EBSD) attached in the SEM machine via an acceleration voltage of 15 kV and step size of 0.1 μ m. In this case, EBSD was run by using OIM Data Collection program and further post-analysis was conducted by TSL OIM Analysis program. Fig. 3 illustrates the EBSD results with various views of the samples after the arranged heat treatments. Fig. 3 (a1, b1, c1 ∼ a4, b4, c4) shows the crystal orientation maps, reconstructed prior austenite grains (PAGs) with statistic distribution attached, kernel average misorientation (KAM) maps and boundary maps of T180, T500 and T650 samples, respectively. It was noted that typical hierarchical structure of lath martensite with PAGs, packets and blocks included was obtained in all the samples as plotted in Fig. 3 (a1), (b1) and (c1). The corresponding boundaries (namely PAGBs, PBs, BBs) were shown by different solid lines. Blocks with similar growth directions were roughly distributed within one packet and different packets within the PAG were tilted in regard to their longitudinal directions. In addition, a random crystal orientation was gathered for the samples irrespective of the tempering temperature. Careful analysis of the reconstructed PAG with statistic data showed a slight uptrend of the PAG size with the increase of tempering temperature. However, the change in PAG size was very limited in view of their average value as shown in Fig. 3 (a2), (b2) and (c2). The observation of KAM maps in Fig. 3 (a3), (b3) and (c3) indicated that the dense spots with high KAM value decreased with the tempering temperature. As for the boundary maps plotted in Fig. 3 (a4), (b4) and (c4), high angle grain boundaries (HAGBs) with misorientation over 15° were basically matched with the PAGBs, PBs and BBs while low angle grain boundaries (LAGBs) with misorientation between 2°∼15° were observed inside the blocks. The statistic data as shown in Fig. 3 (d) again confirmed the decrease in KAM value with the tempering process. As KAM was strongly associated with the local lattice distortion, one would expect the dislocation activities to decrease with the tempering temperature [22,34]. Moreover, no significant difference in the misorientation angle was observed in the samples regarding its statistic distribution as shown in Fig. 3 (e).

To further understand the distribution of subdomain microstructures, careful analysis on the block size and crystal texture of the samples were conducted. Fig. 4 (a1, b1, c1 ∼ a4, b4, c4) shows the extracted blocks with ellipse fitting attached, major axis, minor axis of fitted

Table 1
Main chemical compositions of the material studied in this work (wt.%).

Element	C	Mn	Ni	Cr	Mo	Si	P	S	Cu	Fe
wt.%	0.59	0.79	0.08	1.12	0.15	0.27	0.019	0.012	0.15	Balance

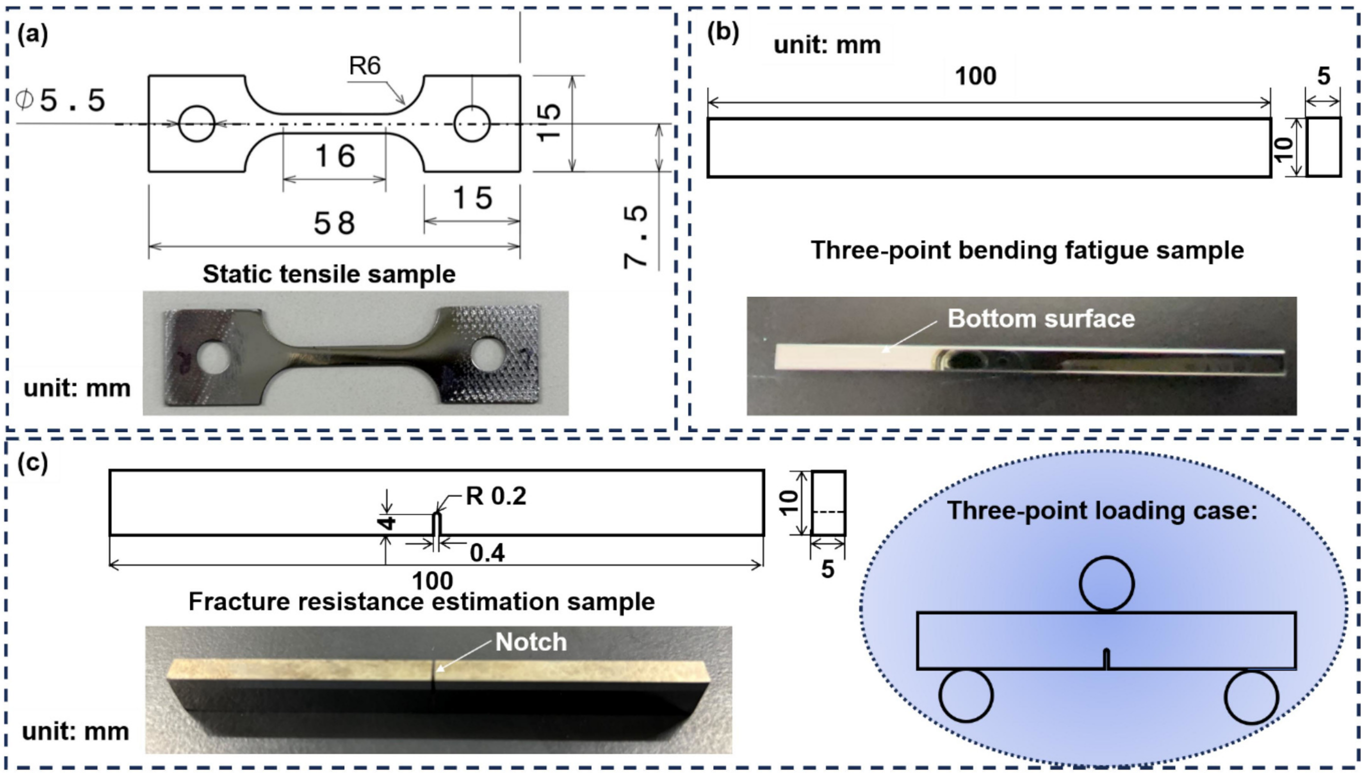

Fig. 1. Shape and dimensions of (a) static tensile sample, (b) three-point bending fatigue sample and (c) fracture resistance estimation sample.

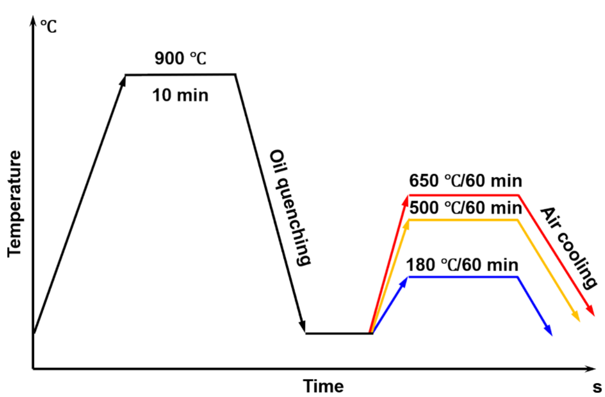

Fig. 2. Heat treatment processes applied in this work.

ellipse and inverse pole figure along various sample directions, respectively. Note that dense blocks emerged in the matrix regardless of tempering temperatures as given in Fig. 4 (a1), (b1) and (c1). The major axis *a* of fitted ellipses indicated slight variation with the tempering temperatures while the change was not appealing as the statistical error was taken into consideration, as noticed in Fig. 4 (a2), (b2) and (c2). In addition, the minor axis *b* of fitted ellipses indicated positive correlation with the major axis and it presented slight increase with the tempering temperature, responsible for global recovery of martensite subdomain blocks, as shown in Fig. 4 (a3), (b3) and (c3). Regarding the inverse pole figures produced along various sample directions, there was no significant texture accumulation observed in all the groups as the maximum texture density was relatively low, as plotted in Fig. 4 (a4), (b4) and (c4).

The etched samples were also observed by SEM to address the carbide precipitation behavior induced by tempering process. An example of the microstructure by various magnifications is shown in Fig. 5. Careful analysis suggested that typical tempered martensite with dispersed small transition carbides (presumably ε-carbides) was the main form of T180 sample, as shown in Fig. 5 (b). As the tempering temperature was increased up to 500 °C, however, dense strip-like carbides (presumably cementite and alloy carbides) were precipitated from the matrix with most visibly and continuously distributed along the boundaries (PAGBs, PBs, BBs), as plotted in Fig. 5 (d). Again, the size of precipitated carbides was increased as a result of further elevation of tempering temperature up to 650 °C. In this case, numerous coarse carbides displayed in a discrete way were visibly observed at the boundaries, as plotted in Fig. 5 (f). Similar findings were also reported in Ref. [35].

2.2. Experimental methods

2.2.1. Static tensile test and fatigue test

The static tensile tests were performed in displacement control with a loading speed of 1 mm/min at room temperature and 2 specimens were tested for each tempering condition. The extensometer was utilized to measure the stain evolution and elongation during the test, and the ultimate tensile strength (UTS) and yield strength (YS) were simultaneously recorded. The three-point bending fatigue tests were implemented under stress-controlled mode by using an electro-hydraulic servo testing machine (SHIMADZU, SFL-50KN-B). A loading ratio of $R = 0.01$ with sinusoidal wave was applied during the fatigue tests to simulate the cyclic bending stress experienced at the gear tooth root during service. In addition, various stress levels selected according to the material properties were utilized for each heat treatment condition and 3 ~ 5 specimens were tested at each stress level to gain the fatigue behavior evolution under different stress levels. It should be noted that the bottom surfaces of all the test samples were manually grounded by sandpapers (No. $80^{\#}$, $320^{\#}$, $500^{\#}$, $1000^{\#}$) and polished by Al_2O_3 (1 μ m) and SiO_2 (0.04 μ m) suspensions before the fatigue. In this regard, the influence of surface roughness and defects on the fatigue behavior can be eliminated. Meanwhile, the edges were also ground to reduce the stress concentration effect.

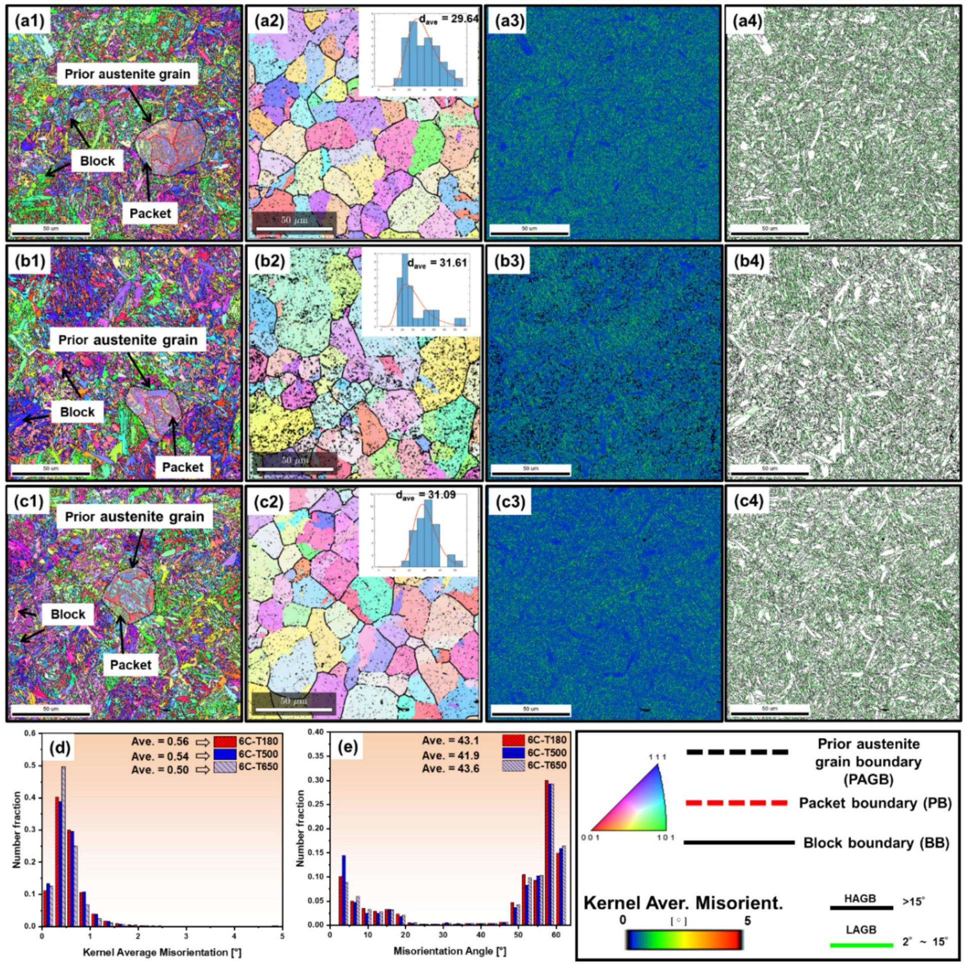

Fig. 3. EBSD analysis of initial microstructures of (a1 ~ a4) T180, (b1 ~ b4) T500, (c1 ~ c4) T650 samples, (d) KAM and (e) misorientation angle distribution of the three group samples. (a1), (b1), (c1) crystal orientation maps, (a2), (b2), (c2) reconstructed prior austenite grains (PAGs) and its distribution, (a3), (b3), (c3) KAM maps, (a4), (b4), (c4) boundary maps. The black frame denotes the correspondence between the value and the featured maps.

2.2.2. *Fracture toughness measurement (FTM) test*

As the tempering process affected the toughness of martensite in an obvious way, this work ran measurement of fracture toughness for each heat treatment condition. The test procedures involved: (i) pre-fabricating micro cracks on the raw notch samples before heat treatment with fatigue loading that followed a maximum stress of 200 MPa and stress ratio of $R = 0.01$, (ii) various heat treatment processes as per Fig. 2 for the crack-existed samples, (iii) accurate measurement of dimensional sizes of samples that were required for further calculation, (iv) quasi-static three-point bending tests for the heat-treated crack-existed samples, (v) careful inspection of pre-crack length and notch length on the fractured samples under each condition, (vi) running calculation of fracture toughness with the data of load and stroke displacement for each sample. To avoid the error, the test was repeated two times for each condition and the average value was compared for further analysis.

2.2.3. *Characterizations*

A SHIMADZU Vickers hardness testing machine with a load of 200 g ($HV_{0.2}$) and duration time of 10 s was applied to gain the hardness evolution under each condition. Tests for each sample were repeated three times and the average estimation was used for further comparison. In addition, the morphologies of fracture surfaces generated in all the mechanical tests were inspected by SEM and part of the fatigue-test samples were analyzed by energy dispersive spectroscopy (EDS) to reveal the mechanisms of fatigue crack initiation behavior.

3. Crystal plasticity finite element method (CPFEM) for fatigue evaluation

3.1. *Demonstration of model details*

In this study, CPFEM was also utilized to evaluate the effect of tempering process on the fatigue behavior of lath martensitic steel. The simulations were performed at uniaxial fatigue, where three types of models namely T180, T500 and T650 were developed in this work. The models were built based on the multi-scale features of lath martensite with prior austenite grains, packets and blocks included. The specific parameters were gained from the EBSD analysis of the initial microstructure for T180, T500 and T650 samples. More importantly, the crystal orientations occurred in the transformation from *parent* austenite to *child* martensite were also taken into consideration during the modelling. The specific procedures for the reconstruction of multi-scale anisotropic tessellations of lath martensite can also be found in previous work [36]. It should be noted that three microstructures were developed for each model during simulation to avoid accidental errors. Fig. 6 gives an example of the microstructures for the reconstructed models of T180, T500 and T650, respectively. Note that the thick dark line represents the PAGB and the thin blue line denotes packet boundary, within which the blocks with different orientations can be observed. After the microstructures were built, they were exported into the finite element software Abaqus and meshed with 8-node hexahedral (C3D8R) elements. Afterwards, they were fully subjected to a cyclic loading stress along the

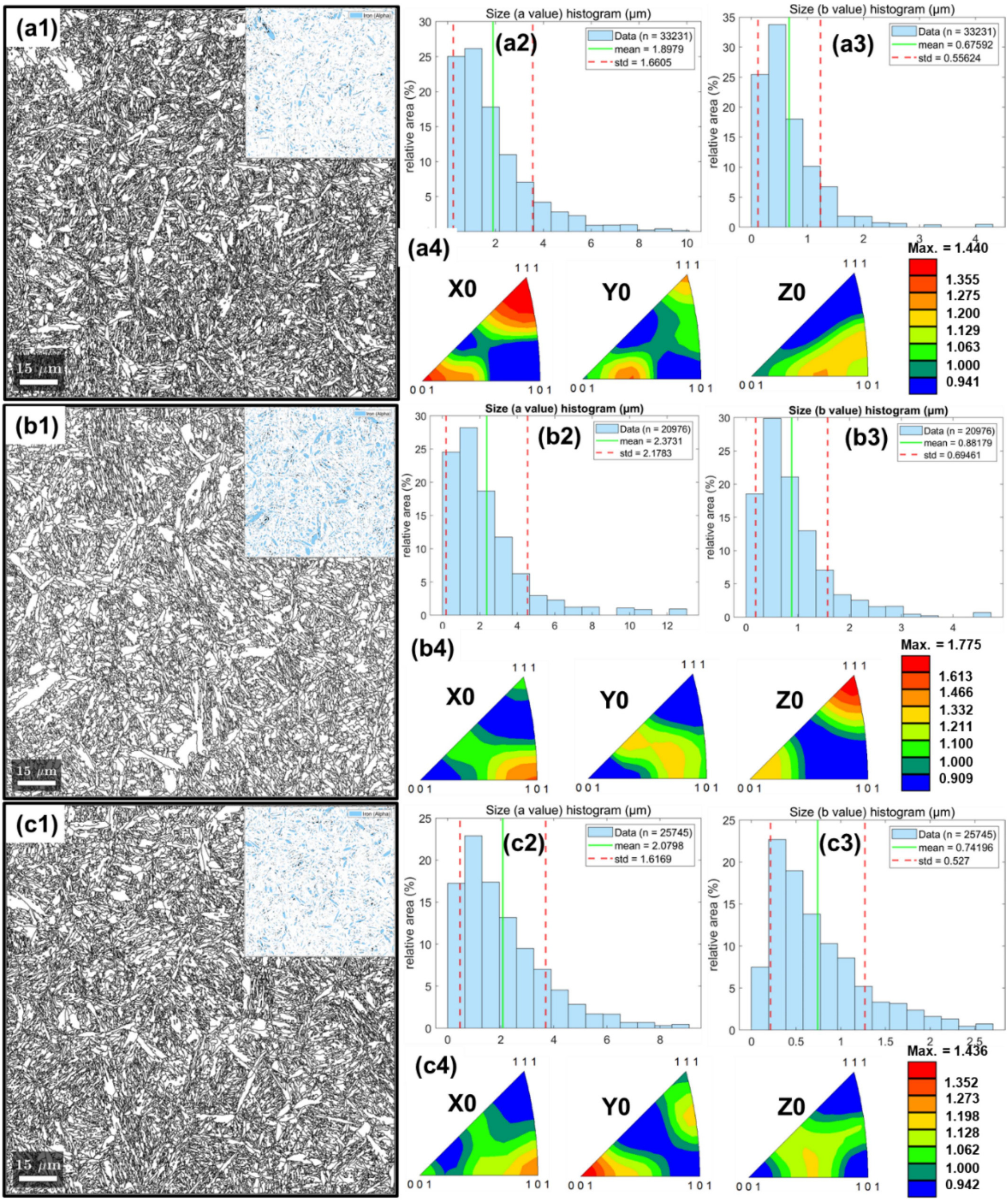

Fig. 4. Post-analysis of subdomain blocks and texture evolution of (a1 ~ a4) T180, (b1 ~ b4) T500 and (c1 ~ c4) T650 samples. (a1), (b1), (c1) recognized blocks and ellipse fitting attached upper right, (a2), (b2), (c2) major axis *a*, (a3), (b3), (c3) minor axis *b* of the fitted ellipse, (a4), (b4), (c4) inverse pole figures along various sample directions.

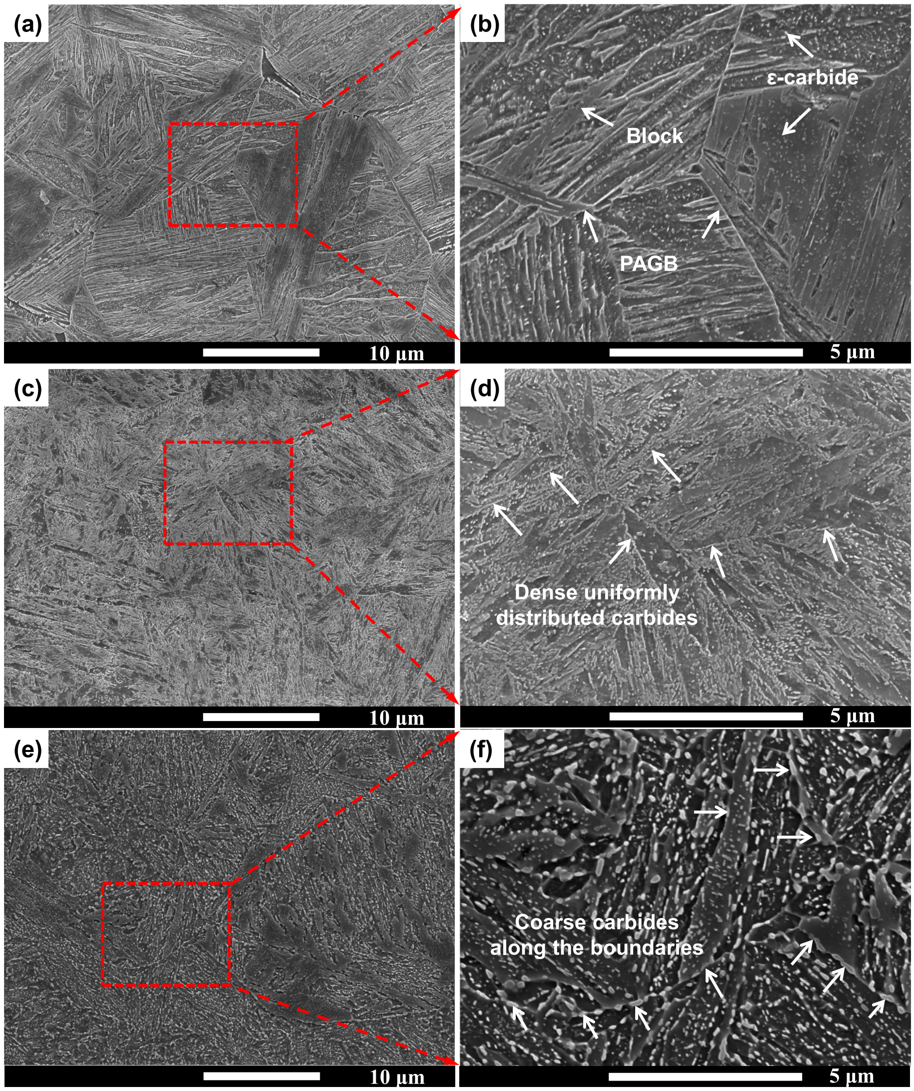

Fig. 5. SEM images of the microstructures of etched (a) T180, (b) T500, (c) T650 samples.

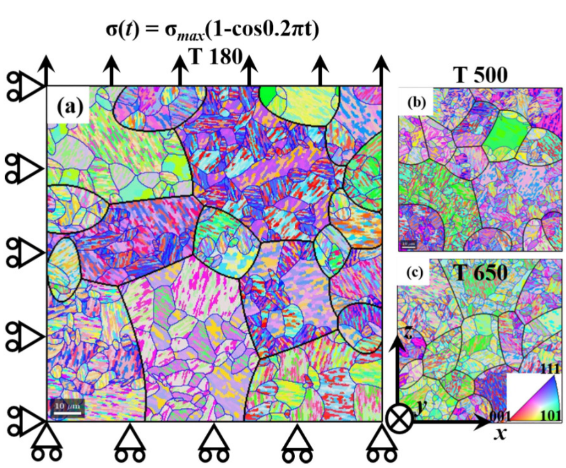

Fig. 6. Reconstructed microstructures of (a) T180, (b) T500 and (c) T650 samples and the corresponding boundary conditions.

z-axis. The boundary conditions regarding the loading status and geometrical constrain were also demonstrated, as shown in Fig. 6. Finally, the results were analyzed on the basis of the last loading cycle of the simulation. The details of the model reconstruction could also be found in our previous work [37].

3.2. Basis of crystal plasticity model

The anisotropic elastoplastic response of crystalline material is governed by their lattice structure and crystallographic orientation. In this study, the investigated material is martensitic steel with a body-centered cubic (BCC) structure. A crystal plasticity model was established within a finite strain framework, where the total deformation gradient $\mathbf{F_t}$ is multiplicatively decomposed into an elastic component $\mathbf{F_e}$ and a plastic component $\mathbf{F_p}$:

$$\mathbf{F}_\mathrm{t} = \mathbf{F}_\mathrm{e}\mathbf{F}_\mathrm{p} \tag{1}$$

It should be noted that, in BCC materials, plastic deformation is primarily governed by dislocation slip occurring on individual slip system α. Accordingly, the plastic velocity gradient can be expressed as:

$$\mathbf{L}_\mathrm{p} = \dot{\boldsymbol{F}}_\mathrm{p}\mathbf{F}_\mathrm{p}^{-1} = \sum\nolimits_{\alpha=1}^{N_{slip}} \dot{\gamma}_s^\alpha \mathbf{m}_s^\alpha \otimes \mathbf{n}_s^\alpha \tag{2}$$

where N_{slip} denotes the total number of active slip systems, $\dot{\gamma}_s^\alpha$ represents the shear strain rate on slip system α, $\mathbf{m}_s^\alpha$ and $\mathbf{n}_s^\alpha$ correspond to the unit vectors of the slip direction and slip plane normal, respectively. In martensite structures, two primary families of slip systems are taken into account, namely {011} < 111 > and {112} < 111 > . The shear strain rate associated with each slip system follows a rate-sensitive power-law formulation [38]:

$$\dot{\gamma}_s^\alpha = \dot{\gamma}_0 \left|\frac{\tau^\alpha}{\tau_c^\alpha}\right|^n \mathrm{sgn}(\tau^\alpha) \tag{3}$$

where $\dot{\gamma}_0$ represents the reference shear strain rate, and n is the strain-rate sensitivity exponent. The quantities τ^α and τ_c^α denote the resolved shear stress and the corresponding critical resolved shear stress (CRSS) on slip system α, respectively. The CRSS evolution accounts for both the initial slip resistance and the subsequent hardening effect, which can be expressed as follows.

$$\tau_c^\alpha = \tau_0^\alpha + \int_t \dot{\tau}_{s\to s}^\alpha dt \tag{4}$$

where τ_0^α denotes the initial slip resistance while $\dot{\tau}_{s\to s}^\alpha$ represents the hardening rate associated with slip interactions, which can be further evaluated as follows.

$$\dot{\tau}_{s\to s}^\alpha = \frac{d\tau_{s\to s}^\alpha}{d\Gamma_s} \sum_{\varsigma=1}^{N_{slip}} h^{\alpha\varsigma} |\dot{\gamma}_s^\varsigma| \tag{5}$$

where Γ_s denotes the total accumulated shear strain over all slip systems, and $h^{\alpha\varsigma}$ characterizes the hardening interaction of slip system ς on slip system α. In addition, a Voce-type hardening law was employed to describe the evolution of the slip resistance [39]:

$$\tau_{s\to s}^\alpha = (\tau_1^\alpha + h_1^\alpha \Gamma_s)(1 - \exp(-\left|\frac{b_1^\alpha}{\tau_1^\alpha}\right|\Gamma_s)) \tag{6}$$

where τ_1^α, h_1^α and b_1^α denote the increment in slip resistance, the saturation value of hardening, and the initial hardening rate for slip system α, respectively.

The parameters of crystal plasticity model were identified and calibrated by calibration against stress–strain curves obtained from quasi-static tensile tests, which provides a reasonable approximation of the material response in the early loading stage for the three types of samples. The parameters of elastic regime for lath martensite were referred from the previous work [38], where $\mathbb{C}_{11} = 268$ GPa, $\mathbb{C}_{12} = 111$ GPa, $\mathbb{C}_{44} = 79$ GPa were utilized. Besides, the reference shear strain rate $\dot{\gamma}_0$ and strain-rate sensitivity exponent n were determined as 0.001 s^{-1} and 20, respectively. The other parameters affected by the material properties are given in Table 2. The simulation results derived from such parameters were compared with the experimental curves, as given in Fig. 7. Note that the simulation curves agree well with the experimental ones, which proves the rationality of the parameters. Besides, it was revealed that lower tempering process enhanced the mechanical strength while the higher tempering process apparently improved the plasticity of the sample.

3.3. Fatigue behavior estimation

In this study, the fatigue crack initiation criterion follows the Tanaka-Mura model, which assumes that crack nucleation occurs on the most favorably oriented slip plane [40]. Accordingly, the number of cycles required for crack initiation N_i could thus be determined concerning the plastic shear strain range $\Delta\gamma$ within a slip band with length l, taking into account the irreversibility of dislocation motion [41]:

Table 2
Crystal plasticity parameters utilized for the models.

Model	τ_0 [MPa]	τ_1 [MPa]	b_1 [MPa]	h_1 [MPa]
T180	800	170	50,000	450
T500	540	30	50,000	120
T650	230	120	50,000	400

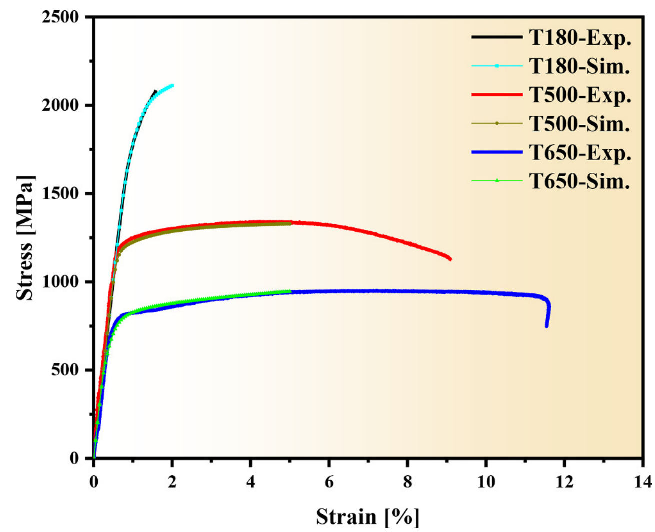

Fig. 7. Stress–strain curves obtained from the CPFEM simulation and experiment for the three types of samples.

$$N_i = \frac{K}{l\left(\Delta\gamma_p/2\right)^2} \tag{7}$$

where K is a material-dependent constant. The plastic shear strain range $\Delta\gamma_p$ represents the shear strain accumulated on a given slip system α during a single loading cycle, and can be expressed as follows:

$$\Delta\gamma_p = \Delta\gamma^\alpha = \int_{(i-1)\Omega}^{i\Omega} |\dot{\gamma}^\alpha| dt \tag{8}$$

where Ω represents the duration of one loading cycle, and the shear strain range is evaluated over the final cycle. In this work, a **fatigue resistance indicator (FRI)** defined on the critical plane for each slip system α is utilized to correlate the local cyclic plastic deformation with the relative tendency for micro fatigue crack initiation under the microstructural effect, which can be expressed as follows [42].

$$FRI = l(\frac{\Delta\gamma^\alpha}{2})^2 \tag{9}$$

In this indicator, a potential crack path (PCP) is defined as the intersection between the slip plane of slip system α and the sample observation plane Multiple parallel PCPs, spaced approximately by the average mesh size, are evaluated within each packet/block. The fatigue behavior is then characterized by the average shear strain range along these PCPs. Similar simulation setup could also be found in our previous work [37].

4. Results

4.1. Characterization of mechanical properties

Fig. 8 gives the microhardness distribution and S-N data plot of samples as a function of tempering temperatures. Note that the highest value of microhardness measured as ~ 780 HV was gained after the oil quenching (OQ) process and tempering reduced the microhardness by releasing the intrinsic stress and promoting dislocation recovery. In this regard, the microhardness indicated visible downtrend with elevation of tempering temperature in view of the average estimation of 690 HV for T180 sample and 300 HV for T650 sample, as plotted in Fig. 8 (a). As for the S-N data, it revealed that the warm tempered samples indicated better fatigue behavior compared to T180 irrespective of the stress levels and the difference in the fatigue life became obvious as a lower load was

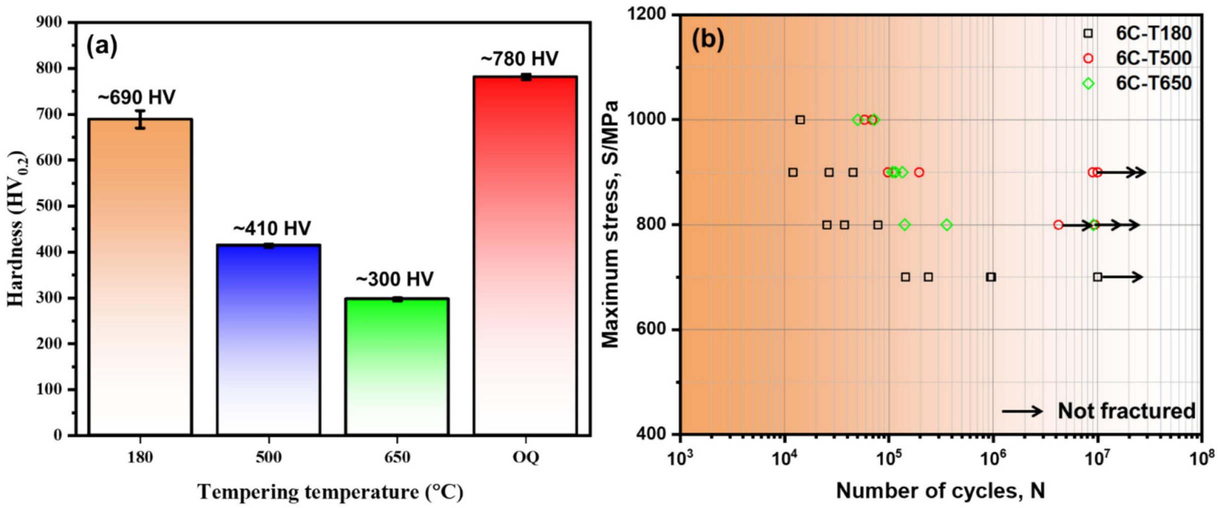

Fig. 8. Mechanical properties of (a) hardness distribution, and (b) S-N data plot of samples under various heat treatment conditions.

applied. In the present work, the cycle number of 10^7 was set as the critical point where the related stress shall be determined as the fatigue limit. It was observed that the highest fatigue resistance was obtained in case of T500 sample since a maximum stress of 900 MPa, under which the sample could survive of 10^7 cycles was at least recorded. Interestingly, the low-tempered samples with relatively high strength presented the worst fatigue resistance where a maximum stress of 700 MPa, under which the sample could survive of 10^7 cycles was captured. These observations demonstrated a strong indication that, for this special configuration, the fatigue behavior of high carbon martensite was considerably dominated by the plasticity, instead of only strength mattered, the mechanism of which will be further discussed.

4.2. Fracture surface observations

Fig. 9 shows SEM images of fracture surfaces of tensile tests with different heat treatment conditions. Careful analysis of the morphologies showed that brittle fracture emerged in an intragranular way was predominant in the fracture surface of T180 sample, as plotted in Fig. 9 (a). However, ductility fracture with visible plastic dimples and steps was the main form in fracture surfaces of T500 and T650 samples, as seen in Fig. 9 (b) and (c). Meanwhile, obvious necking trace was noticed in these two cases which again confirmed the superior plasticity of warm tempered martensitic steels.

The SEM images of crack propagation region with insert images showing the pre-crack and notch during the fracture resistance measurement were also recorded, as plotted in Fig. 10. Visible difference along the interface indicated that the crack proceeded in varying manner with the change of tempering process. To be specific, the crack propagated immediately in an intergranular way once it was formed for T180 sample, as shown in Fig. 10 (a). Apparently, intragranular fracture with numerous dimples was the way that the crack was emerged in the early propagation area for T500 and T650 samples, as noticed in Fig. 10 (b) and (c). Moreover, voids with random visible inclusions inside were also observed, which confirmed the presence of precipitations during the metallurgical process of studied material in this work. The insert images with clear difference in various areas were used to measure the crack length, i.e. the total length of notch and pre-crack under each condition.

Fig. 11 plots the SEM images of fatigue fracture surfaces of T180 samples under various stress levels. Starting with the analysis of fracture surfaces under high load, obvious crack initiation and propagation regions were captured (see Fig. 11a1). Inclusions accompanied with facet fracture here were the crack initiation source in this case as plotted in Fig. 11 (a2). Again, the cracks basically propagated in an intergranular way in the early/stable propagation regions as shown in Fig. 11 (a3). As the crack arrived at the quick propagation area, numerous cleavage faces with shallow dimples were observed. Moreover, some strip-like inclusions were noticed along the fracture surface (see Fig. 11 a4). As the stress levels were lower, the crack initiations adjacent to the surface were again clearly noticed (see Fig. 11 b1). Apparently, carbides and inclusions that act as the stress concentration points accelerated the crack nucleation as shown in Fig. 11 (b2). As the cracks started to propagate, they still preferred to proceed in an intergranular way (see Fig. 11 b3). In this case, grain debonding due to the weak boundary strength occurred to accommodate the plastic strain (see Fig. 11 b4). As the load was further reduced, a better fatigue life was achieved while the mechanism responsible for crack initiation and propagation was not changed. Carbides and inclusions at the topmost surface caused the initiation (see Fig. 11 c1, c2). Cracks tended to propagate in an intergranular manner and grain debonding was randomly distributed at this stage as shown in Fig. 11 (c3), (c4). These results provided evidence that brittle fracture can be dominantly activated in fatigue process, which probably deteriorated the fatigue resistance of the low-tempered sample.

As high temperature tempering was performed, the fracture behavior

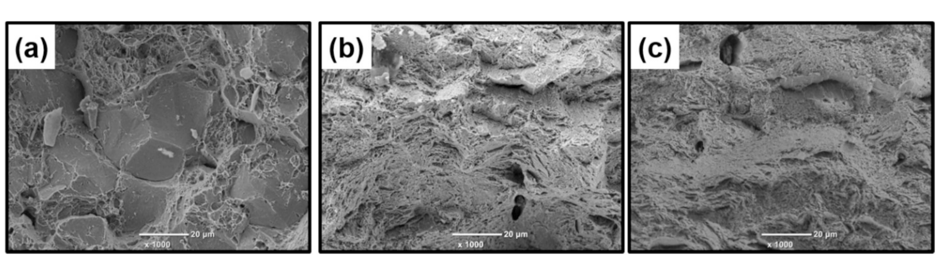

Fig. 9. Fracture surfaces of tensile tests observed with different magnifications: (a) T180, (b) T500, (c) T650.

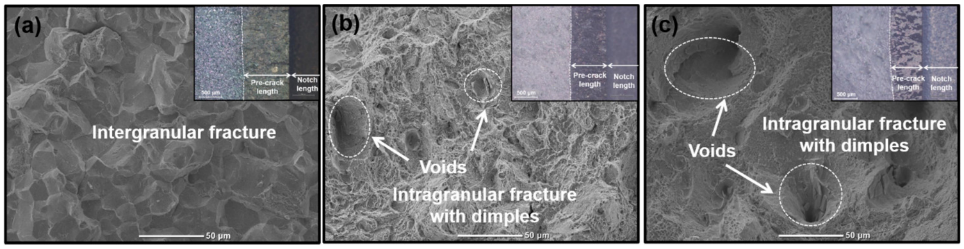

Fig. 10. SEM images of crack propagation region observed in toughness measurement of (a) T180, (b) T500, (c) T650 samples with insert images showing the pre-crack and notch.

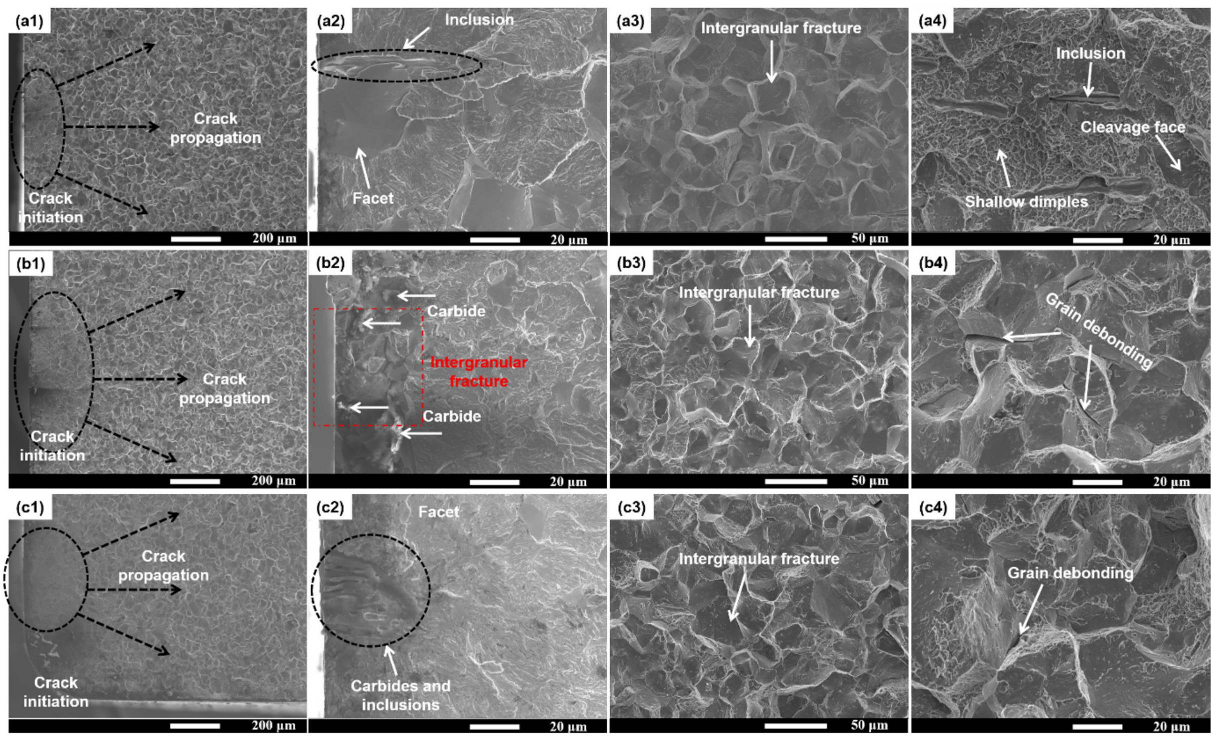

Fig. 11. SEM images of typical fatigue fracture surfaces of T180 sample under various stress levels: (a1) ~ (a4) S = 1000 MPa, N = 14187, (b1) ~ (b4) S = 900 MPa, N = 12008, (c1) ~ (c4) S = 700 MPa, N = 959544.

during fatigue was revealed to be totally different. This was nicely illustrated in Fig. 12 where crack initiation and the early/stable

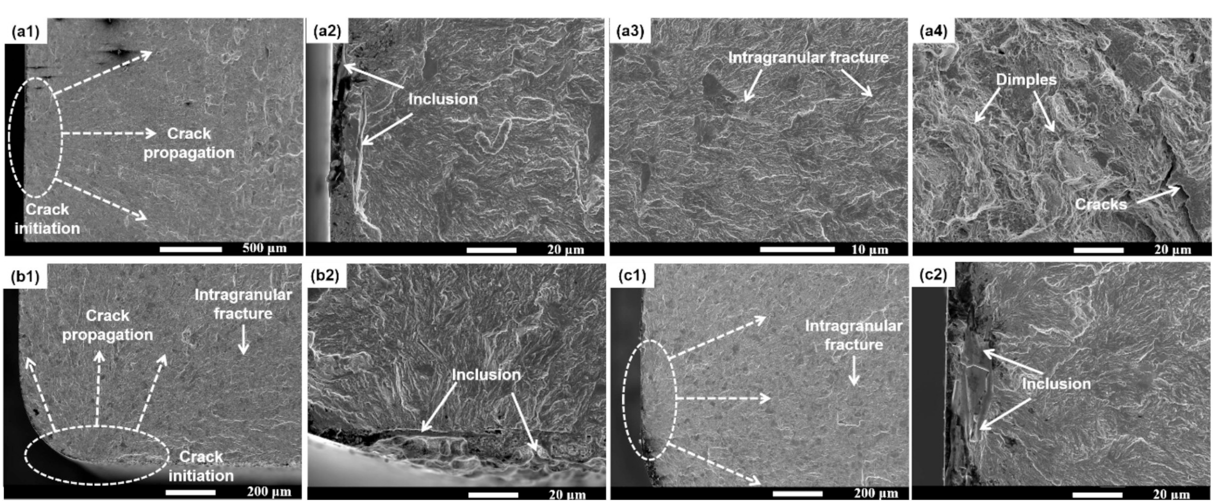

Fig. 12. SEM images of typical fatigue fracture surfaces of T500 sample under various stress levels: (a1) ~ (a4) S = 1000 MPa, N = 69155, (b1), (b2) S = 900 MPa, N = 194823, (c1), (c2) S = 900 MPa, N = 98047.

propagation features were shown. Starting from the analysis of fracture with high stress, clear signs of cracks initiated from inclusions were noticed (see Fig. 12 a1, a2). Interestingly, the cracks initially propagated in an intragranular instead of intergranular way in this case, as seen in Fig. 12 (a3). As the crack arrived at the quick propagation area, numerous dimples along with secondary cracks occurred (see Fig. 12 a4). As the applied load was reduced, for example with stress of 900 MPa, the inclusions were still revealed as candidates for crack initiation of the fractured samples, and their probability for crack initiation seemed statistically determined (see Fig. 12 b2, c2). In this regard, the samples were not broken probably if the inclusions were reasonably excluded at the test surface, which was presented in the S-N plot (see the not fractured samples at the same stress).

Fig. 13 plots the fracture surfaces of T650 sample subjected to various stress levels. Similarly, the cracks initiated from the inclusions at the topmost surface as the load was high. In this case, tearing edge was also noticed owing to the low strength of the test material (see Fig. 13 a1, a2). As the crack penetrated into the quick propagation area, dimples along with inclusions and carbides were observed (see Fig. 13 a3, a4). Again, the inclusions were revealed as source of crack initiation even though the stress was lower (see Fig. 13 b1, b2). However, cracks needed time to proceed with striations emerged in this case and dimples induced by plastic fracture occurred during propagation (see Fig. 13 c1, c2).

5. Discussions

5.1. Mechanical properties evolution with tempering temperatures

Previously, the microstructure responses as a function of tempering processes of high carbon martensitic steels were clarified by several characterizations. Careful analysis suggested that the PAG size slightly increased with the tempering temperature while the variation was rather limited. The fitted ellipses of blocks indicated that there was a marginal elevation in the block size especially in case of block width with the tempering process while the change was not appealing. Moreover, dislocation density reduced with the elevation of tempering temperature as supported by the KAM evolution in Fig. 3. These results were similar to those seen in the study of low carbon martensitic steels by different tempering processes in Refs. [22,25,43]. More precisely, the reason could be ascribed to the enhancement of recovery ability of dislocations under the softening effect of high temperatures. More importantly, the SEM observations provided a strong indication that the segregation of carbon atoms responsible for the attractive carbide formation with higher tempering mode was considerably activated as shown in Fig. 5. All these behaviors, therefore, could lead to an obvious difference in the mechanical responses of the studied materials as evidenced by the variation of strength as well as microhardness.

In general, the yield strength of high strength steel could be estimated as a result of multiple strengthening contributions as denoted by Eq. (10) [44].

$$\sigma_y = \sigma_0 + \sigma_s + \sigma_{dis} + \sigma_p + \sigma_d \tag{10}$$

where σ_0, σ_s, σ_{dis}, σ_p, σ_d presented the intrinsic lattice friction stress, solid solution strengthening, dislocation strengthening, precipitation strengthening, and grain boundary strengthening, respectively. To be specific, the lattice friction stress was inherently determined for the pure bcc iron (~50 MPa) [15]. As the main strengthening mechanism of high carbon steel, the value of solid solution strengthening could be estimated as a function of the soluble carbon content as expressed as [45]

$$\sigma_s = k_s C_s \tag{11}$$

where k_s denoted a material constant and C_s was the amount of soluble carbon atoms (wt.%) of tempered martensite. The contribution of dislocations on the strength could be determined by the Taylor hardening law as expressed by Eq. (12) [46]:

$$\sigma_{dis} = M\alpha G b\sqrt{\rho_t} \tag{12}$$

where M, α, G, b, ρ_t denoted Taylor factor, empirical constant, shear modulus, Burgers vector and dislocation density, respectively. As for the possible strengthening mechanism of carbon steel, the precipitation effect could be presented on the basis of Orowan dislocation bypassed behavior as described in Eq. (13) [47]:

$$\sigma_P = 0.538\frac{Gb}{D_p}f_P^{1/2}\ln\frac{D_p}{2b} \tag{13}$$

where G, b, D_p, f_p denoted the shear modulus, magnitude of Burgers vector, real diameter of the particles, and volume fraction of precipitations, respectively. Finally, the grain boundary induced strengthening effect could be determined based on the Hall-Petch relationship as given in Eq. (14) [48]:

$$\sigma_d = k_d \cdot d^{-1/2} \tag{14}$$

where k_d and d were empirical constant and effective grain size of test material, respectively.

In this work, the martensitic steel with a lower tempering temperature (T180) presented a relatively high strength while the ductility was

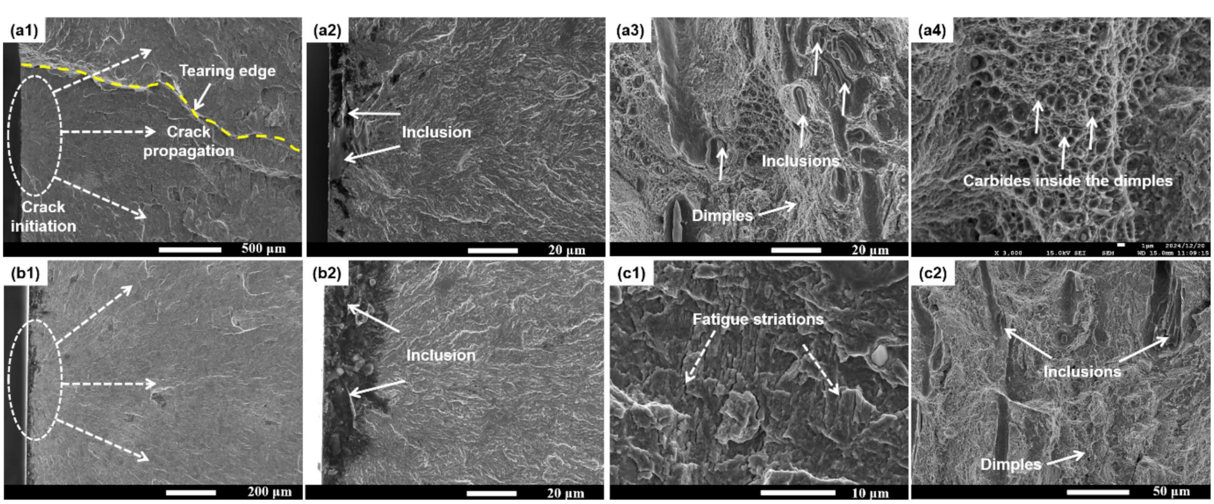

Fig. 13. SEM images of typical fatigue fracture surfaces of T650 sample under various stress levels: (a1) ~ (a4) S = 1000 MPa, N = 72294, (b1), (b2) S = 900 MPa, N = 115800, (c1), (c2) S = 800 MPa, N = 358550.

poor. The relevant reasons involved in that: (i) carbon atoms in solid solution provided strong strengthening effect by pinning the dislocations in this case [49]. (ii) A high number of dislocations generated during quenching were still maintained at lower tempering mode which also contributed to the work hardening. (iii) Careful analysis of the microstructures as given in Fig. 5 (b) showed that numerous fine carbides were dispersed in the matrix in the high carbon steel, which provided precipitation hardening by hindering the dislocation movement [11,47]. (iv) The finer lath martensite grains with a large amount of high angle boundaries could act as formidable obstacles to plastic low, which strengthened the material [44,50]. Therefore, the plastic work was restrained which enhanced the strength and hardness of the material while weakened the ductility.

However, the behavior of carbon atoms in solid solute was changed with higher tempering process, which caused an obvious difference in the material property. In general, dislocations could be regarded as a trap for carbon atoms and carbon segregation usually appeared toward the crystal defects [35,51]. Thus, it was reasonably speculated that the release of carbon atoms due to dislocation annihilations upon higher tempering shall accelerate the carbide precipitation, where it might easily happen along the boundaries. This agreed well with the case in T500 sample as plotted in Fig. 5 (d). In other words, the redistribution of solute carbon atoms at either boundaries or matrix could result in a depleted carbon content in the grain interiors as compared to the nominal composition. Therefore, the solid solution strengthening and work hardening effects were simultaneously deteriorated in this case as estimated by Eq. (11) and (12) [52]. Instead, the softening upon higher tempering, to some extent, could also be compensated by the precipitation hardening of dense carbides, which reduced the trade-off degree in strength while maintaining superior ductility [53]. Nevertheless, coarse carbides that grew further were discontinuously distributed along the boundaries in case of T650 sample as given in Fig. 5 (f). To this end, the precipitation hardening effect was not much pronounced as depicted by Eq. (13). Moreover, plasticity along boundaries were previously characterized as one of the main mechanisms in martensite deformation [54–56]. Thus, the presence of coarse carbides at boundaries may render boundaries even more susceptible for localized plastic deformation in this case [49]. Apart from the mentioned behaviors, the slight increase in effective grain size at higher tempering temperature also deteriorated the strength as depicted by Eq. (14). Here, extensive recovery that

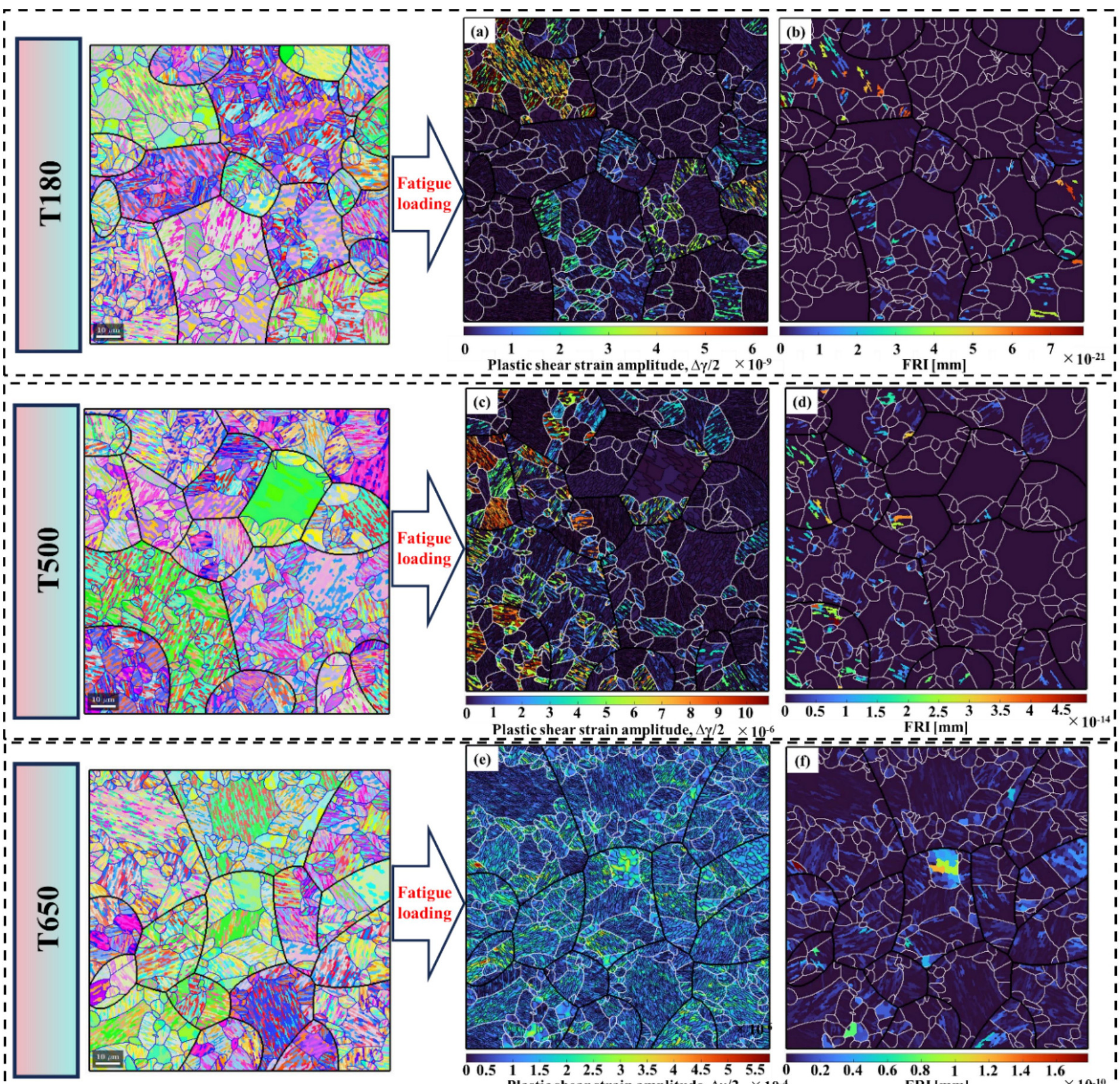

Fig. 14. Distribution of plastic shear strain amplitude and FRI accumulated in the last simulated cycle for (a), (b) T180, (c), (d) T500 and (e), (f) T650 samples.

softened the high angle boundaries at higher tempering process would not hinder the dislocation motion as obvious as that tempered in a low mode, which further promoted the ductility for such material.

As the microhardness has coherent relation with the yield strength, one would expected the microhardness to be predicted by following the Tabor's empirical formula [57]:

$$\sigma_y = CH_v \tag{15}$$

where C was a constant in the range of 2.5 ~ 3 (MPa/HV) [44], which was estimated to be 2.6 in this work and H_v denoted the Vickers microhardness value. In this work, the microhardness after various tempering processes was obtained from Vickers indentations which probed an μm-sized interaction comprising several types of boundaries and inherent matrix of martensite. In such way, the magnitude is a rather representative measure of the mechanical response of the entire martensitic microstructure [49]. In this work, the microhardness indicated a linear downward trend with the tempering temperature which matched well with the evolution of yield strength as plotted in Fig. 8.

5.2. Fatigue behavior characterizations with tempering temperatures

It has been known that the material microstructure affected the fatigue behavior of metals in view of slips [58,59]. The relevant mechanisms which accounted for the difference in crack initiation behavior were firstly revealed by simulations. Fig. 14 presents the distribution of plastic shear strain amplitude and the proposed FRI accumulated in the last simulated cycle for samples under various tempering processes from CPFEM analysis. It was clear that the shear strain distribution indicated strong heterogeneities subjected to the fatigue loading irrespective of the tempering temperature, which shall be affected by the crystallographic orientations, as plotted in Fig. 14 (a), (c) and (e). High shear strain tended to develop at specific blocks along their longitudinal direction, which indicated that fatigue crack initiation in martensite was closely associated with its multiscale hierarchical microstructure. Similar findings were also reported in Ref. [36] in the simulation of fatigue behavior of low carbon martensitic steel. More specifically, tempering temperature significantly altered the distribution of local shear strain. In the low-tempered condition, the martensite retained a high dislocation density, which caused high strength and a large resistance to slip. In addition, the martensitic microstructure remained highly heterogeneous. Thus, slips were restricted to limited regions within the blocks that possessed favorable crystallographic orientations, and the magnitude of local shear strain was relatively low (see Fig. 14 a). As the tempering temperature increased up to 500 °C, microstructural recovery occurred and the internal dislocation activities decreased. The corresponding reduction in strength lowered the resistance to slip, making plastic deformation easier to activate within certain blocks. As a result, local shear strain became more concentrated and its magnitude increased (see Fig. 14 b). When the tempering temperature was further increased, substantial softening appeared accompanied by a marked reduction in dislocation density and a pronounced decrease in slip resistance. The overall capacity for plastic deformation was therefore enhanced. In this case, the shear strain distribution became more homogeneous, while the strain magnitude was generally higher throughout the microstructure (see Fig. 14 e).

Regarding the proposed FRI, its spatial distribution was broadly similar to that of shear strain field and also exhibited pronounced heterogeneities. However, FRI additionally incorporated the effect of slip band length, which represented the formation of a continuous strain-localization path. Therefore, this parameter provided a more physically relevant assessment of driving force for fatigue crack initiation. Table 3 summarizes the average values of top ten maximum FRI obtained from three models for each microstructure configuration. In the low-tempered condition, only a few blocks exhibited relatively high FRI values, indicating that potential fatigue crack initiation was confined to these specific regions. Nevertheless, the overall magnitude was low, suggesting that crack initiation was still difficult under this case. With the elevation of tempering temperature, particularly in T650 case, the FRI distribution became more homogeneous and its magnitude increased markedly. This behavior indicated that the number of potential candidates for fatigue crack initiation obviously increased. Overall, these results suggested that high tempering process reduced the resistance to crack initiation by promoting more widespread and more intense slip-related local damage. However, such slip-induced crack initiation behavior was not the dominant mechanism responsible for the final fatigue life regarding the experimental S-N data plot. Further analysis is needed to explore the effect of tempering process on the fatigue behavior of high carbon martensitic steel.

Table 3
The average values of top ten maximum FRI from three models for each microstructural configuration.

Sample	T180 [mm]	T500 [mm]	T650 [mm]
Model 1	$6.45 \bullet 10^{-21}$	$3.38 \bullet 10^{-14}$	$7.87 \bullet 10^{-11}$
Model 2	$9.60 \bullet 10^{-21}$	$3.26 \bullet 10^{-14}$	$5.69 \bullet 10^{-11}$
Model 3	$6.21 \bullet 10^{-21}$	$5.67 \bullet 10^{-14}$	$6.59 \bullet 10^{-11}$
Ave.	$7.42 \bullet 10^{-21}$	$4.10 \bullet 10^{-14}$	$6.72 \bullet 10^{-11}$

Usually, fracture toughness as affected by the inherent material property also played an essential role in the fatigue failure of high strength steels [60]. Although martensitic steels offered high strength, their relative low toughness particularly in high carbon case could facilitate crack propagation under cyclic loading [61]. Therefore, the estimation of fracture resistance was also carried out via the way shown in section 2.2.2 to reveal the mechanisms that governs the fatigue failure. Fig. 15 shows the evolution of load F applied with the stroke displacement l for the test samples. Note that an appealing increase in the maximum load at failure was captured with higher tempering temperatures (T500 and T650) as compared to the low mode (T180). This result confirmed that under higher tempering process resistance to crack propagation of high carbon martensite was much higher. In this work, the equations used to calculate the fracture toughness value were shown as [62,63]:

$$K_Q = \left(\frac{F_{\max}S}{BW^{3/2}}\right) \times f\left(\frac{a}{W}\right) \tag{16}$$

And in the case of $0 < a/W < 1$:

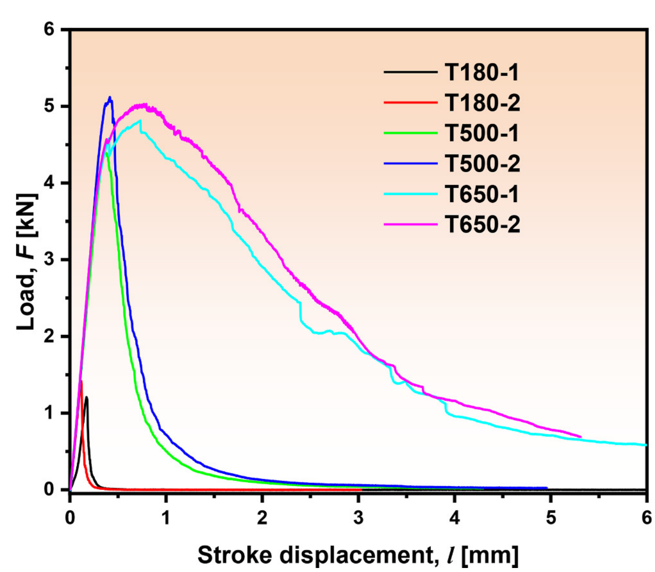

Fig. 15. Load-displacement curves during FTM tests for different samples with varying tempering temperatures.

$$f(\frac{a}{W}) = 3(\frac{a}{W})^{1/2} \times \frac{1.99 - (\frac{a}{W})(1-\frac{a}{W})\left[2.15 - 3.93(\frac{a}{W}) + 2.70(\frac{a}{W})^2\right]}{2(1+2\frac{a}{W})(1-\frac{a}{W})^{3/2}} \quad (17)$$

where a, W, F_{max}, B, S were the crack length, sample height, maximum load at failure, sample width, distance between two supporting rollers, respectively. Finally, the specific value of each parameter and the calculated fracture toughness values according to ASTM E399 are shown in Table 4. It can be noted that fracture toughness of T500 and T650 samples was higher (considerably 3.5 times) as compared to T180. This again confirmed that the high resistance to crack propagation instead of poor strength at higher tempering processes would dominantly result in an enhancement of the fatigue resistance in T500 and T650 samples as verified by the S-N plot in Fig. 8.

To further address the mechanisms responsible for the delay in fatigue failure at higher tempering mode, the evolution of stroke displacement and its differentiation versus the fatigue cycle number (i.e. stroke velocity, dl/dN) were simultaneously recorded as shown in Fig. 16. Starting with the analysis at the same high stress level (see Fig. 16 a, c, e), it indicated that the stroke displacement changed abruptly at a certain cycle number which caused a sharp increase in the stroke velocity for T180 sample as given in Fig. 16 (a). However, the stroke displacement presented a transitional increase before the final failure for T500 and T650 samples, resulting in a gradual elevation of stroke velocity as given in Fig. 16 (c), (e). As the load was reduced, similar phenomenon in regard to the stroke displacement and its velocity was noticed for T180 sample as given in Fig. 16 (b). These results provided evidence that a very weak resistance to cracks in T180 sample led to premature fatigue failure, which was nicely supported by the low K_Q as given in Table 4. In other words, the sample would fracture very soon even though a small slip-induced crack was only formed in this case and brittle fracture emerged in a catastrophic manner shall dominate the failure. However, there was still an obvious transition in the stroke displacement for T500 and T650 samples before the final fracture. Also, a fluctuation adjacent to the final fracture was captured in the stroke velocity, which seemed to be a sign of crack propagation in this case, as shown in Fig. 16 (d), (f). These results proved that high K_Q of T500 and T650 samples enhanced the resistance to early crack growth, which delayed the cycles before the fast crack propagation. In this regard, the intragranular fracture with obvious fatigue striations dominated the early crack propagation, which lead to a better fatigue behavior as compared to T180 sample.

Here, the cracks formed during fatigue process for each type of sample were also observed and typical plots at certain cycles are given in Fig. 17. It was clear that the T180 sample experienced brittle fracture with relatively straight failure trace once the crack occurred, which matched the critical point of variation of stroke velocity (see Fig. 17 a2). However, there was an attractive growth trace of crack which thus induced the formation of one big crack before the failure in case of T500 sample (see Fig. 17 b2, b3). In other words, the big crack formation that accounted for a very high fraction of the entire fatigue life dominated the final failure in this case. Due to the high conditional fracture toughness of T500 sample, the resistance to the formation of big crack that was defined as "main crack initiation life" here was strongly enhanced, thereby resulting in an overall exceptional fatigue resistance.

Similar findings in case of main crack before fracture were also noticed in T650 sample. However, the difference was that two cracks co-existed and one of them was revealed as the candidate of final fracture (see Fig. 17 c2, c3). This behavior can be ascribed to the relatively low strength of T650 sample as shown in Fig. 7, where slipping might easily happen owing to the corresponding low critical resolved shear stress (CRSS). Thus, more small cracks could be easily activated under the cyclic loading and their possibility for growing as a big crack was statistically determined. Consequently, the fatigue resistance in this case was slightly reduced as compared to T500 sample (see S-N plot).

5.3. Fatigue failure mechanisms

Based on the above observations and discussions, the fatigue failure mechanisms induced from the tempering processes of high carbon martensitic steels was concluded. Fig. 18 illustrates a schematic diagram of the crack formation for each type of sample, with special attention paid on the main crack trace responsible for the final fatigue failure. In the case of T180 sample, the hard carbides and/or inclusions at boundaries or grain interior that caused stress concentration usually acted as nucleation sites for crack. Moreover, some previous studies claimed that the transformation from blocky retained austenite to martensite owing to local plastic deformation under cyclic loading could also induce the formation of micro cracks [64]. Considering the numerous defects in high carbon martensite, dense dislocations displayed in the networks and walls shall contribute to the strain localization under external loading, which accelerated the formation of micro cracks [65]. Once the micro crack appeared, it propagated very fast due to the low fracture toughness of this type of material. Specifically, the cracks preferred to proceed in an intergranular way due to the weak grain boundaries and their macroscopic paths presented a nearly perpendicular spatial orientation to the loading direction as depicted in Fig. 18 (a). These results provided indication that the underlying microstructure of high carbon martensite sample dominantly motivated the brittle crack propagation over the stress intensity threshold value under cyclic loading, which was also reported in Ref. [66]. In the case of T500 sample, the MnS inclusions were revealed as the main crack initiation mechanisms according to the SEM analysis of the fractured samples, which was similar with the findings in our previous work [37]. Nevertheless, some scholars also found that the cracks predominantly formed along packet and block boundaries while MnS inclusions have minimal effect on the crack formation [67]. Therefore, it was reasonably hypothesized that the slipping induced small cracks represented by extrusions and intrusions were also candidates for crack nucleation considering the lower yield strength (i.e. considerably critical resolved shear stress) of the T500 sample [68,69], which has been proved by the CPFEM simulation. However, much high energy was needed to trigger the crack growth due to the high conditional fracture toughness of this type of material, which significantly slowed down the crack growth rate and delayed the cycles toward the main crack formation. Also, dense carbides acted as obstacles in the crack growth, under which the crack closure might happen and thus the small cracks were annihilated before becoming the main crack as plotted in Fig. 18 (b). This behavior nicely supported the cases of unfractured samples with the same stress level if the MnS inclusions were excluded as given in the S-N plot. In the case of

Table 4
Parameters and calculated fracture toughness values for different sample conditions.

Sample	F_{max}/kN	S/mm	B/mm	W/mm	a/mm	a/W	$f(a/W)$	Fracture toughness/ MPa·m$^{1/2}$	Designation
T180, #1	1.208	40	5.015	10.057	5.2588	0.522899	2.867217	27	K_{IC}
T180, #2	1.418	40	5.011	10.042	5.0945	0.507319	2.725445	31	K_{IC}
T500, #1	4.392	40	5.021	10.006	5.1011	0.509804	2.747329	96	K_Q
T500, #2	5.116	40	5.017	9.997	4.9181	0.491958	2.59584	106	K_Q
T650, #1	4.815	40	5.027	10.000	4.9312	0.49312	2.605318	100	K_Q
T650, #2	5.022	40	5.042	10.051	4.9454	0.492031	2.596434	103	K_Q

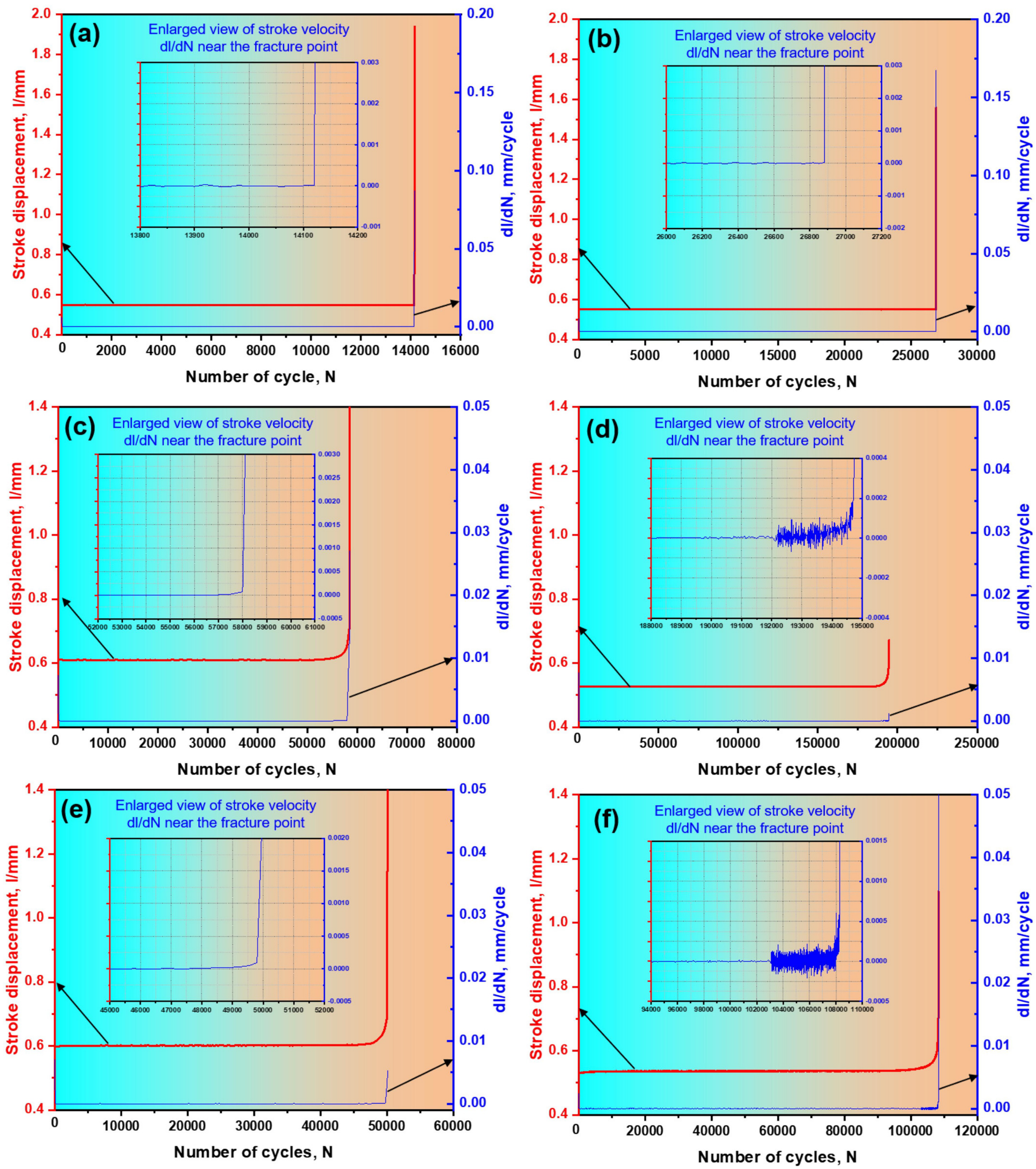

Fig. 16. Stroke displacement and velocity (dl/dN) during the fatigue process of (a), (b) T180, (c), (d) T500, (e), (f) T650 samples. (a), (c), (e) and (b), (d), (f) denote the results at a stress level of 1000 MPa and 900 MPa, respectively.

T650 sample, the combination of coarse carbides along boundaries and MnS inclusions that caused stress concentration triggered the crack initiation based on the SEM observations. Moreover, multiple slipping-induced micro cracks were easily initiated under the cyclic loading owing to its poor yield strength, as supported by CPFEM simulation. As the micro cracks were formed, high energy may still be consumed to promote their growth because of the high conditional fracture toughness associated with this material. Also, the coarse carbides may act as barriers during the crack growth which sometimes lead to crack closure [70]. However, there was an obvious reduction in the strength in T650 sample compared to T180 and T500 samples owing to excessive tempering as mentioned in Fig. 7. This behavior increased the possibility of further crack growth with the help of dislocation movement as the solute and boundary strengthening was weak in this case. In this regard,

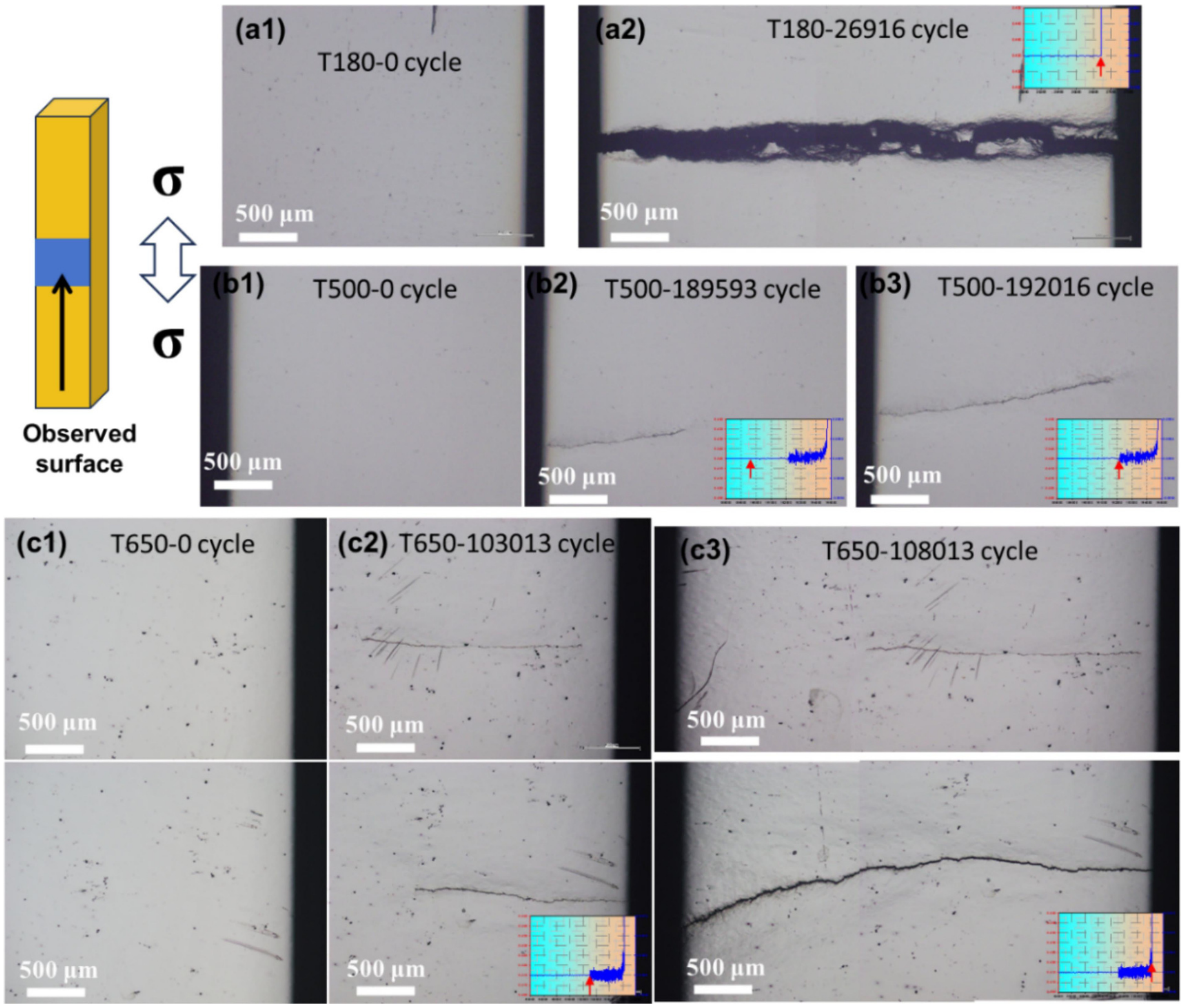

Fig. 17. In-situ crack observation during fatigue process for (a1), (a2) T180, (b1), (b2), (b3) T500, (c1), (c2), (c3) T650 samples at a stress of 900 MPa. The corresponding cycle numbers with respect to stroke velocity re marked in the attached images.

several main cracks could be simultaneously triggered, which led to premature failure of the sample. Thus, the fatigue resistance was somehow reduced even though the conditional fracture toughness was high. These results provided evidence that, for this particular configuration, the good combination of high conditional fracture roughness and considerable strength via quenching and tempering at 500 °C resulted in an exceptional fatigue resistance.

6. Conclusions

In summary, a 0.6% C martensitic steel was subjected to quenching followed by different tempering treatments, and the resulting microstructural evolution and mechanical responses were systematically investigated, with particular emphasis on fatigue behavior. Based on the results, the main conclusions are drawn as follows:

- A slight increase in prior austenite grain size and martensite block size was observed at higher tempering temperatures, while the overall variation remained limited. Enhanced carbon segregation at elevated temperatures promoted the precipitation of dense carbides along boundaries.
- Low-temperature tempering resulted in higher strength and hardness at the expense of ductility, whereas high-temperature tempering significantly reduced strength and hardness but improved elongation, indicating a clear strength–ductility trade-off.
- Carbides and inclusions were identified as the primary crack initiation sites under all tempering conditions. However, low-tempered samples exhibited predominantly intergranular brittle fracture, while high-tempered samples showed intragranular crack propagation characterized by fatigue striations.
- The fatigue resistance of the 0.6C martensitic steel was primarily governed by fracture toughness, which controls the transition from microstructural damage (e.g. slip activity and microcracks) to main crack formation. Higher tempering temperatures enhanced conditional fracture toughness and delayed the main crack formation, thereby extending fatigue life. However, excessive tempering reduced strength and increased the number of potential main crack formation sites, which may ultimately compromise fatigue performance.

CRediT authorship contribution statement

Jiaqiang Dang: Writing – original draft, Validation, Methodology, Investigation, Formal analysis, Conceptualization. **Sien Liu:** Resources, Formal analysis, Data curation. **Eisuke Kazama:** Formal analysis, Data curation. **Ryuji Yabutani:** Resources, Methodology. **Karel Blanken:** Visualization, Resources. **Fabien Briffod:** Resources, Methodology. **Shoichi Nambu:** Writing – review & editing, Supervision, Project administration, Funding acquisition.

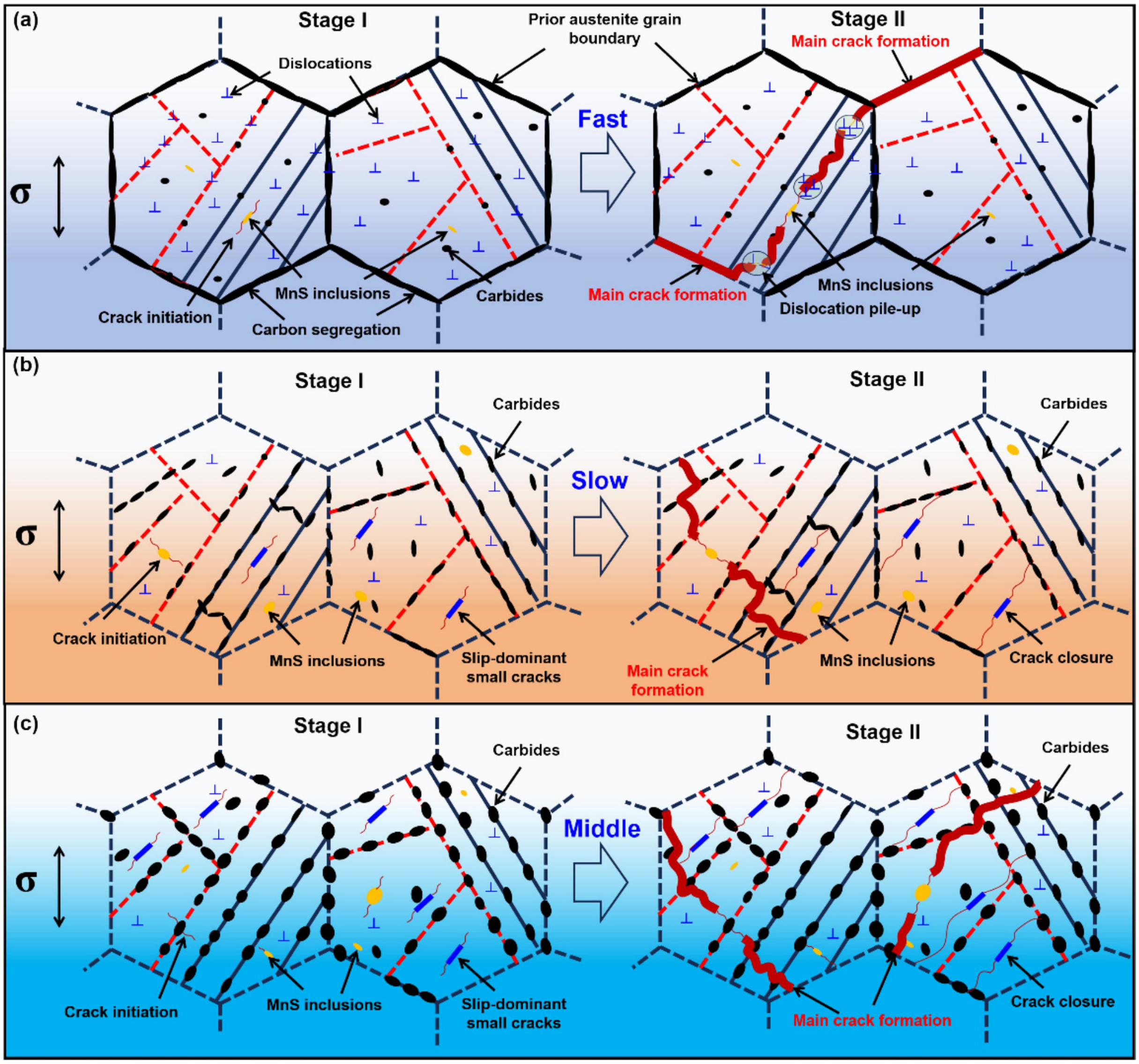

Fig. 18. Schematic diagram of the crack formation in (a) T180, (b) T500, (c) T650 samples. Stage I ~ Stage II denotes the process of main crack formation responsible for the final fatigue failure.

Declaration of competing interest

The authors declare that they have no known competing financial interests or personal relationships that could have appeared to influence the work reported in this paper.

Acknowledgement

This paper is supported by Green Innovation Fund Projects (JPNP21026) commissioned by the New Energy and Industrial Technology Development Organization (NEDO).

Data availability

Data will be made available on request.

References

[1] Qin S, Zhang C, Zhang B, Ma H, Zhao M. Effect of carburizing process on high cycle fatigue behavior of 18CrNiMo7-6 steel. J Mater Res Technol 2022;16:1136–49.
[2] Zhang Y, Wang S, Xu G, Wang G, Zhao M. Effect of microstructure on fatigue-crack propagation of 18CrNiMo7-6 high-strength steel. Int J Fatigue 2022;163:107027.
[3] Xiao B, Yadav SD, Zhao L, Tang Z, Han Y, Yang X, et al. Deep insights on the creep behavior and mechanism of a novel G115 steel: Micromechanical modeling and experimental validation. Int J Plast 2021;147:103124.
[4] Qin S, Wang L, Di L, Zhang C, Zhao M. Effect of carburizing process on bending fatigue performance of notched parts of 18CrNiMo7-6 alloy steel. Eng Fail Anal 2023;147:107161.
[5] Zhang Y, Sang X, Xu G, Wang G, Zhao M. Fatigue crack propagation of the gradient surface-modified layer of high-strength steel. Int J Fatigue 2023;177:107921.
[6] Liu S, Shimizu K, Dang J, Blanken K, Briffod F, Nambu S. Improving the ductility of 2.6-GPa high-carbon martensitic steel by prior bainitic transformation. Mater Sci Eng A 2026;957:149955.
[7] Qin S, Feng M, Tian Q, Song Z, Zhao M. Influence of cold treatment on fatigue performance of 18CrNiMo7-6 carburized steel. Int J Fatigue 2024;183:108242.
[8] Yao Z, Hao J, Dai W, Li C, Zhang H, Zhang Y. Effects of quenching medium and tempering temperature on microstructure, mechanical properties, and fatigue behavior of EA4T steel. Int J Fatigue 2022;165:107179.
[9] Guo S, Li C, Shi J, Luan F, Song X. Effect of quenching media and tempering temperature on fatigue property and fatigue life estimation based on RBF neural network of 0.44 % carbon steel. Mech Sci 2019;10(1):273–86.
[10] Zheng H, Yang Y, Li J, Zuo X, Wan J, Rong Y, et al. Mechanisms of secondary crack initiation, propagation and closure during the water quenching process in medium-carbon martensitic steel. Int J Plast 2025;185:104240.
[11] Tao Q, Wang J, Galindo-Nava EI. Effect of low-temperature tempering on confined precipitation and mechanical properties of carburised steels. Mater Sci Eng A 2021;822:141688.
[12] Lai C, Huang W, Li S, Liu T, Lv R, Tang X, et al. Effects of quenching and tempering heat treatment on microstructure, mechanical properties, and fatigue crack growth behavior of 51CrV4 spring steel. Mater Res Express 2021;8(9):096514.

[13] Zheng H, Zhang J, Zuo X, Rong Y, Wan J, Chen N. Multi-interface migration mechanism induced by carbide precipitation during the quenching-partitioning-tempering process in a high-carbon steel. Int J Plast 2024;175:103928.
[14] Peng J, Zhou B, Li Z, Huo D, Xiong J, Zhang S. Effect of tempering process on the cryogenic impact toughness of 13Cr4NiMo martensitic stainless steel. J Mater Res Technol 2023;23:5618–30.
[15] Wang J, Tao Q, Fan J, Fu L, Shan A. Enhanced mechanical properties of a high-carbon martensite steel processed by heavy warm rolling and tempering. Mater Sci Eng A 2023;872:144958.
[16] Zhang Y, Zhan D, Qi X, Jiang Z. Effect of tempering temperature on the microstructure and properties of ultrahigh-strength stainless steel. J Mater Sci Technol 2019;35(7):1240–9.
[17] Wang Z, Huang MX. Optimising the strength-ductility-toughness combination in ultra-high strength quenching and partitioning steels by tailoring martensite matrix and retained austenite. Int J Plast 2020;134:102851.
[18] Li H, Jing H, Xu L, Han Y, Zhao L, Tang Z, et al. Fatigue behavior, microstructural evolution, and fatigue life model based on dislocation annihilation of an Fe-Ni-Cr alloy at 700 °C. Int J Plast 2019;118:105–29.
[19] Dhua SK, Mukerjee D, Sarma DS. Effect of cooling rate on the as-quenched microstructure and mechanical properties of HSLA-100 steel plates. Metall Mater Trans A 2003;34(11):2493–504.
[20] Rani SU, Preethi M. Effect of tempering temperature and time on microstructure and mechanical properties of 26MnB5 martensitic steel tubes. Procedia Struct Integrity 2019;14:142–9.
[21] Zhao Y-j, Ren X-p, Hu Z-l, Xiong Z-p, Zeng J-m, Hou B-y. Effect of tempering on microstructure and mechanical properties of 3Mn-Si-Ni martensitic steel. Mater Sci Eng A 2018;711:397–404.
[22] Yang G, Xia SL, Zhang FC, Branco R, Long XY, Li YG, et al. Effect of tempering temperature on monotonic and low-cycle fatigue properties of a new low-carbon martensitic steel. Mater Sci Eng A 2021;826:141939.
[23] Zhao Y, Tong X, Wei XH, Xu SS, Lan S, Wang XL, et al. Effects of microstructure on crack resistance and low-temperature toughness of ultra-low carbon high strength steel. Int J Plast 2019;116:203–15.
[24] Morra PV, Radelaar S, Yandouzi M, Chen J, Böttger AJ. Precipitate coarsening-induced plasticity: low temperature creep behaviour of tempered SAE 52100. Int J Plast 2009;25(12):2331–48.
[25] Qu S-G, Zhang Y-L, Lai F-Q, Li X-Q. Effect of tempering temperatures on tensile properties and rotary bending fatigue behaviors of 17Cr2Ni2MoVNb steel. Metals 2018;8(7):507.
[26] Zhang Z, Delagnes D, Bernhart G. Ageing effect on cyclic plasticity of a tempered martensitic steel. Int J Fatigue 2007;29(2):336–46.
[27] Wei DY, Gu JL, Fang HS, Bai BZ, Yang ZG. Fatigue behavior of 1500 MPa bainite/martensite duplex-phase high strength steel. Int J Fatigue 2004;26(4):437–42.
[28] Kwon H, Barlat F, Lee M, Chung Y, Uhm S. Influence of tempering temperature on low cycle fatigue of high strength steel. ISIJ Int 2014;54(4):979–84.
[29] Delagnes D, Rézaï-Aria F, Levaillant C. Influence of testing and tempering temperatures on fatigue behaviour, life and crack initiation mechanisms in a 5%Cr martensitic steel. Procedia Eng 2010;2(1):427–39.
[30] Cheng Z, Zhang C, Guo J, Yan J, Li S, Wang S, et al. Effect of microstructural features on the fatigue behavior of ultra-high strength press hardened steels. J Mater Res Technol 2024;32:1192–205.
[31] Yu W, Qian L, Wei C, Li K, Ding Y, Yu P, et al. Enhancing the ductility and yield strength of 2.7Mn steel via two-step partitioning heat treatment. Int J Plast 2024;183:104148.
[32] Morito S, Tanaka H, Konishi R, Furuhara T, Maki T. The morphology and crystallography of lath martensite in Fe-C alloys. Acta Mater 2003;51(6):1789–99.
[33] Ryou KH, Nambu S, Koseki T. Effect of carbon content on selection of slip system during uniaxial tensile deformation of lath martensite. Mater Sci Eng A 2020;777:139090.
[34] Dang J, Zhang H, An Q, Ming W, Chen M. On the microstructural evolution pattern of 300 M steel subjected to surface cryogenic grinding treatment. J Manuf Process 2021;68:169–85.
[35] Clarke AJ, Miller MK, Field RD, Coughlin DR, Gibbs PJ, Clarke KD, et al. Atomic and nanoscale chemical and structural changes in quenched and tempered 4340 steel. Acta Mater 2014;77:17–27.
[36] Briffod F, Shiraiwa T, Enoki M. Modeling and crystal plasticity simulations of lath martensitic steel under fatigue loading. Mater Trans 2018;60(2):199–206.
[37] Dang J, Yabutani R, Liu S, Nambu S. Microstructure and bending fatigue behavior of martensite steel with 0.4%C subjected to different heat treatments. Int J Fatigue 2025;197:108910.
[38] Briffod F, Shiraiwa T, Yamazaki K, Enoki M. Integrated experimental–numerical investigation of strain partitioning and damage initiation in a low-carbon lath martensitic steel. Mater Sci Eng A 2023;876:145148.
[39] Briffod F, Hu H, Shiraiwa T, Enoki M. Effect of in-lath slip strength on the strain partitioning in a dual-phase steel investigated by high-resolution digital image correlation and crystal plasticity simulations. Mater Sci Eng A 2023;862:144413.
[40] Tanaka K, Mura T. A dislocation model for fatigue crack initiation. J Appl Mech 1981;48(1):97–103.
[41] Alexandre F, Deyber S, Pineau A. Modelling the optimum grain size on the low cycle fatigue life of a Ni based superalloy in the presence of two possible crack initiation sites. Scr Mater 2004;50(1):25–30.
[42] Briffod F, Shiraiwa T, Enoki M. Microstructure modeling and crystal plasticity simulations for the evaluation of fatigue crack initiation in α-iron specimen including an elliptic defect. Mater Sci Eng A 2017;695:165–77.
[43] Saastamoinen A, Kaijalainen A, Heikkala J, Porter D, Suikkanen P. The effect of tempering temperature on microstructure, mechanical properties and bendability of direct-quenched low-alloy strip steel. Mater Sci Eng A 2018;730:284–94.
[44] Mao G, Cao R, Cayron C, Mao X, Logé R, Chen J. Effect of cooling conditions on microstructures and mechanical behaviors of reheated low-carbon weld metals. Mater Sci Eng A 2019;744:671–81.
[45] Seol J-B, Jung JE, Jang YW, Park CG. Influence of carbon content on the microstructure, martensitic transformation and mechanical properties in austenite/ε-martensite dual-phase Fe–Mn–C steels. Acta Mater 2013;61(2):558–78.
[46] He BB, Hu B, Yen HW, Cheng GJ, Wang ZK, Luo HW, et al. High dislocation density–induced large ductility in deformed and partitioned steels. Science 2017;357(6355):1029–32.
[47] Gladman T. Precipitation hardening in metals. Mater Sci Technol 1999;15(1):30–6.
[48] Dang J, Wang H, Wang C, An Q, Li Y, Wang H, et al. Microstructure evolution and surface strengthening behavior of 300 M ultrahigh strength steel under engineered surface treatments. Mater Charact 2024;215:114127.
[49] Morsdorf L, Kashiwar A, Kübel C, Tasan CC. Carbon segregation and cementite precipitation at grain boundaries in quenched and tempered lath martensite. Mater Sci Eng A 2023;862:144369.
[50] Dang J, Zhang H, An Q, Lian G, Li Y, Wang H, et al. Surface integrity and wear behavior of 300M steel subjected to ultrasonic surface rolling process. Surf Coat Technol 2021;421:127380.
[51] Wilde J, Cerezo A, Smith GDW. Three-dimensional atomic-scale mapping of a cottrell atmosphere around a dislocation in iron. Scr Mater 2000;43(1):39–48.
[52] Seol J-B, Raabe D, Choi P-P, Im Y-R, Park C-G. Atomic scale effects of alloying, partitioning, solute drag and austempering on the mechanical properties of high-carbon bainitic–austenitic TRIP steels. Acta Mater 2012;60(17):6183–99.
[53] Morsdorf L, Emelina E, Gault B, Herbig M, Tasan CC. Carbon redistribution in quenched and tempered lath martensite. Acta Mater 2021;205:116521.
[54] Du C, Hoefnagels JPM, Vaes R, Geers MGD. Plasticity of lath martensite by sliding of substructure boundaries. Scr Mater 2016;120:37–40.
[55] Morsdorf L, Jeannin O, Barbier D, Mitsuhara M, Raabe D, Tasan CC. Multiple mechanisms of lath martensite plasticity. Acta Mater 2016;121:202–14.
[56] Du C, Petrov R, Geers MGD, Hoefnagels JPM. Lath martensite plasticity enabled by apparent sliding of substructure boundaries. Mater Des 2019;172:107646.
[57] Mao G, Cao R, Cayron C, Logé R, Guo X, Jiang Y, et al. Microstructural evolution and mechanical property development with nickel addition in low-carbon weld butt joints. J Mater Process Technol 2018;262:638–49.
[58] Song K, Xu L, Zhao L, Han Y, Xiao B, Ma N. A microstructurally-sensitive damage model considering grain boundary effect under fatigue and creep-fatigue interaction. Int J Plast 2025;194:104484.
[59] Dang J, Liu S, Yabutani R, Nambu S. Effect of Mo, Ni additions and carburized treatments on the surface microstructure and bending fatigue behavior of SCM420H steel. Int J Fatigue 2026;205:109429.
[60] Li HF, Wei JL, Yang SP, Liu YQ. The relationship between fracture toughness and tensile property in high-strength steels. Eng Fail Anal 2022;131:105854.
[61] Liu L, Li L, He J, Liang Z, Peng Z, Gao J, et al. The unexpected low fracture toughness of dual-phase steels caused by ferrite/martensite interface decohesion. Scr Mater 2024;244:116030.
[62] Srawley JE. Wide range stress intensity factor expressions for ASTM E 399 standard fracture toughness specimens. Int J Fract 1976;12(3):475–6.
[63] Roberts JC, Merkle AC, Carneal CA, Voo LM, Johannes MS, Paulson JM, et al. Development of a human cranial bone surrogate for impact studies. Front Bioeng Biotechnol 2013;1–2013.
[64] Gao G, Zhang B, Cheng C, Zhao P, Zhang H, Bai B. Very high cycle fatigue behaviors of bainite/martensite multiphase steel treated by quenching-partitioning-tempering process. Int J Fatigue 2016;92:203–10.
[65] Zhang X, Wang T, Gong X, Li Q, Liu Y, Wang Q, et al. Low cycle fatigue properties, damage mechanism, life prediction and microstructure of MarBN steel: influence of temperature. Int J Fatigue 2021;144:106070.
[66] Koschella K, Krupp U. Investigations of fatigue damage in tempered martensitic steel in the HCF regime. Int J Fatigue 2019;124:113–22.
[67] Sierra-Soraluce A, Li G, Santofimia MJ, Molina-Aldareguia JM, Smith A, Muratori M, et al. Exploring the effect of complex hierarchic microstructure of quenched and partitioned martensitic stainless steels on their high cycle fatigue behaviour. Mater Des 2023;233:112286.
[68] Seidametova G, Vogt; J-B, Proriol SI. The early stage of fatigue crack initiation in a 12%Cr martensitic steel. Int J Fatigue 2018;106:38–48.
[69] Li X, Dai Y, Wang X, Liu Y, Chen Y, Wang C, et al. Effects of local microstructure on crack initiation in super martensitic stainless steel under very-high-cycle fatigue. Int J Fatigue 2022;163:107019.
[70] Zhang J, Chen H, Fu H, Cui Y, Wang C, Chen H, et al. Retarding effect of submicron carbides on short fatigue crack propagation: mechanistic modeling and experimental validation. Acta Mater 2023;250:118875.